

Photon absorption in twisted bilayer graphene

Disha Arora, Deepanshu Aggarwal, Sankalpa Ghosh and Rohit Narula
Department of Physics, Indian Institute of Technology Delhi, New Delhi-110016, India

We investigate one- and two-photon absorption in twisted bilayer graphene (TBLG) by examining the effects of tuning the twist angle θ and the excitation energy E_l on their corresponding absorption coefficients $\alpha_{i=1,2}$. We find that α_1 shows distinct peaks as a function of E_l which correspond to the van Hove singularities (vHS) of TBLG. In contrast to single- (SLG) and AB bilayer graphene (BLG), α_1 is substantially enhanced by ~ 2 and ~ 1 orders of magnitude, respectively, in the visible range. On the other hand, α_2 exhibits a remarkable increase of ~ 11 and ~ 9 orders of magnitude. Interestingly, as θ increases, the resonant features exhibited by $\alpha_{i=1,2}$ *vs.* E_l shift progressively from the infrared to the visible. On doping TBLG, both α_1 and α_2 remain essentially unchanged *vs.* E_l but with a minor red-shift in their resonant peaks. Additionally, we explore various polarization configurations for TPA and determine the conditions under which α_2 becomes extremal.

I. INTRODUCTION

Twisted bilayer graphene (TBLG) is a two-dimensional superlattice [1–7] formed when a pair of stacked graphene layers are relatively rotated about the base AB bilayer graphene (BLG) configuration. This twisting gives rise to a moiré pattern [8] with localized *AA* and *AB*-rich regions that form a moiré lattice. The interlayer interaction between the misoriented layers significantly modifies the low energy band structure thus endowing it with distinctive electrical [9, 10] and optical properties [11–19]. By tuning the twist angle, the location of the van-Hove singularities (vHS) can be varied [5, 20, 21] without the introduction of defects, chemical doping or electrical gating. At small twist angles *e.g.*, $\theta \sim 1.05^\circ$, TBLG exhibits almost flat energy bands [22–29], thus enabling features like unconventional superconductivity [30–32] and Mott insulating states [33–39].

Multiphoton absorption [41, 42] (MPA) processes in crystalline solids have been the focus of much theoretical and experimental research [43–45]. Particularly at short wavelengths, nonlinear absorption is a key factor in limiting the transparency of optical window materials and in producing laser-induced damage to optical components [41]. In general, these processes typically involve all of the solid’s energy bands as intermediate states, so even a single MPA experiment can provide detailed information about the energy-band structure when combined with other pertinent experimental or theoretical data [46–51] that is not easily obtained by using linear techniques. To enable a transition from the ground to the excited state by the simultaneous absorption of two photons, the material is excited using a light source that has a wavelength which is nearly twice that of linear absorption. As a result, while the two photon absorption (TPA) rate grows with the square of the photon flux, the one-photon absorption (OPA) rate depends linearly on the intensity [52]. Due to the low photon energy involved in TPA, the material under high penetration sustains less damage. TPA plays a crucial role in laser spectroscopy by enabling the transition between two states that are not able to be coupled by an electric-dipole interaction [53–

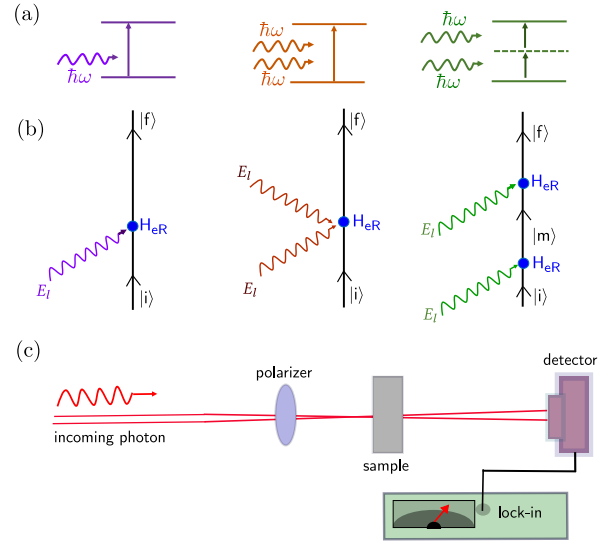


FIG. 1. Schematic for (a) one photon absorption and two-photon absorption in simultaneous, and step-wise scheme, respectively. (b) The corresponding Feynman diagrams and (c) Schematic of the experimental setup for absorption process [40].

55]. It has been demonstrated [56] that quantum interference between OPA and TPA can solve the coherent control [57] and non-contact generation of ballistic photocurrent in multilayer graphene, which have applications in quantum technology. TPA can also enable coherently excited states of molecules with energies in the far ultraviolet [58] when using visible light, for which coherent sources are conveniently available. Indeed, TPA provides a way of accessing a given excited state with the use of photons of half the energy (or twice the wavelength) of the corresponding one-photon transition, thus leading to applications in microscopy, micro-fabrication [59], three-dimensional data storage [60, 61], optical power limiting [62], two-photon fluorescence imaging [63] and sensing [64]. Unlike other nonlinear all-optical processes such as second harmonic generation [65], TPA has the benefit of generating a direct electrical response to the optical sig-

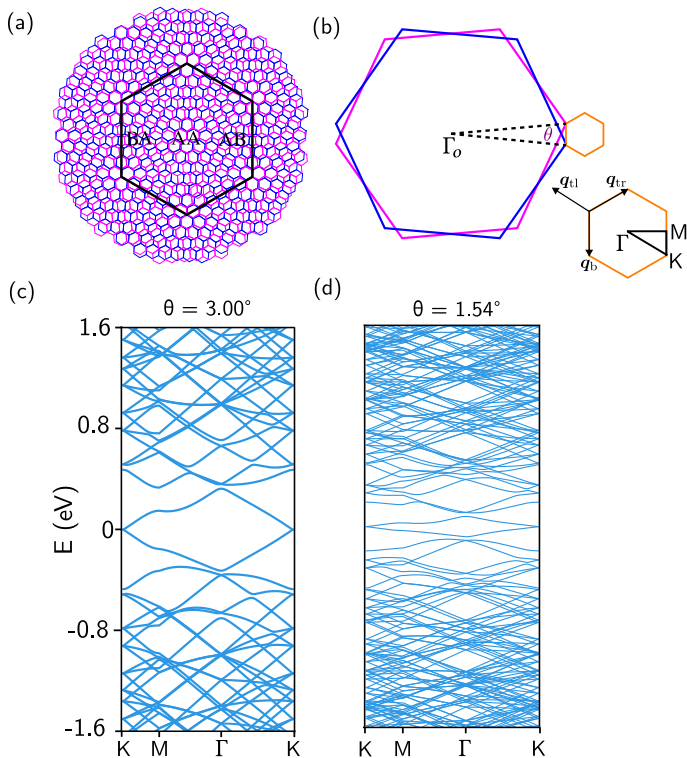


FIG. 2. A two-dimensional view of TBLG in (a) real space and (b) reciprocal space, respectively. The small orange hexagon outlines the MBZ. The band structure along the high-symmetry path of MBZ and DOS for twist angles (c) $\theta = 3.00^\circ$ (d) $\theta = 1.54^\circ$. The w parameters are taken from Ref. [67].

nal without the need for phase matching. As a result, it's also used to second-order autocorrelation, which lets one calculate optical logic operations and pulse duration [66].

The absorption of photons is an elementary process to all the higher-order processes involving light-matter interactions like Raman scattering [68, 69], one-, two- or three-photon scattering [41, 70], *etc.* In this paper we study the polarization-controlled absorption characteristics of TBLG, specifically focusing on the absorption of one- and two-photons. We explore the effects of tuning the twist angle θ and the excitation energy E_l on their corresponding absorption coefficients $\alpha_{i=1,2}$. According to our findings, when compared to single-layer graphene (SLG) and unrotated bilayer graphene (BLG), α_1 experiences an enhancement of ~ 2 and 1 orders of magnitude, respectively, in the visible range. In contrast, the magnitude of α_2 undergoes a remarkable enhancement of ~ 11 and 9 orders of magnitude. This giant increase ought to be of considerable importance since it enables various applications in fields such as photovoltaic [71], photo detectors [72], medical imaging [73], *etc.* Interestingly, the resonant features exhibited by the absorption coefficients progressively shift from the infrared to the visible part of the energy spectrum. Furthermore, we delve various polarization configurations for the two photons

independently, determining the conditions under which α_2 becomes extremal.

This paper is organized as follows: Sec. II discusses the theory of multi-photon absorption process and provides the relevant expressions used in our calculations. The interaction of photons with TBLG is discussed and derived in Sec. III. In section. IV we discuss the behavior of the OPA and TPA coefficients as a function of the incoming photon energy. Our conclusions and its scope of future work are outlined in Sec. V.

II. THEORETICAL BACKGROUND

Theoretically, both the so-called microscopic and macroscopic techniques have been used to study MPA [41]. In the former, the photon-induced electronic transition probabilities are used to compute the absorption coefficients, whereas in the latter they are derived from the imaginary part of the macroscopic current operator \mathbf{j} [74, 75]. In Appendix A, based on Refs [76, 77], we evaluate the macroscopic current operator and the absorption coefficients for TBLG. For our purposes, to calculate the absorption coefficients within the microscopic picture we follow the approach developed by Göppert-Mayer [78] in which the n^{th} -order time-dependent perturbation theory is employed to derive an expression for the probability of the simultaneous absorption of n photons by a single atomic electron. Applying this elementary idea to a crystalline material provides the probability of a direct electronic transition from an initial valence band v to a final conduction band c , accompanied by the simultaneous absorption of n photons, each of frequency ω and is given as [41, 79, 80]:

$$W_n = \frac{2\pi}{\hbar} \int_{\mathbf{k}} |\mathcal{T}|^2 \delta[E_c(\mathbf{k}) - E_v(\mathbf{k}) - n\hbar\omega] \frac{d^3\mathbf{k}}{(2\pi)^3} \quad (1)$$

where,

$$\mathcal{T} = \sum_{m \dots i} \frac{\langle \psi_c | H_{eR} | \psi_m \rangle \langle \psi_m | H_{eR} | \psi_l \rangle \dots \langle \psi_i | H_{eR} | \psi_v \rangle}{E_m - E_l - (n-1)\hbar\omega \dots E_i - E_v - \hbar\omega} \quad (2)$$

W_n is the n^{th} order transition probability rate per unit volume. $\psi_i, \psi_j \dots$ are the Bloch functions of the crystalline electrons in bands $i, j \dots$ with energies $E_i, E_j \dots$ respectively. Energy conservation is expressed by the delta function δ and the summation is taken over all the possible intermediates states for a given transition. The summation over \mathbf{k} is carried over the entire first Brillouin zone. $H_{eR} = \frac{e}{c} \mathbf{A} \cdot v_F \boldsymbol{\sigma}$ is the electron-radiation interaction Hamiltonian, where $\mathbf{A} = A\mathbf{e}$ is the vector potential of the incoming light wave of amplitude A and polarization vector \mathbf{e} . The n -photon absorption coefficient is related to the n^{th} -order transition probability as

$$\alpha_n = \frac{2W_n n \hbar \omega}{I^n} \quad (3)$$

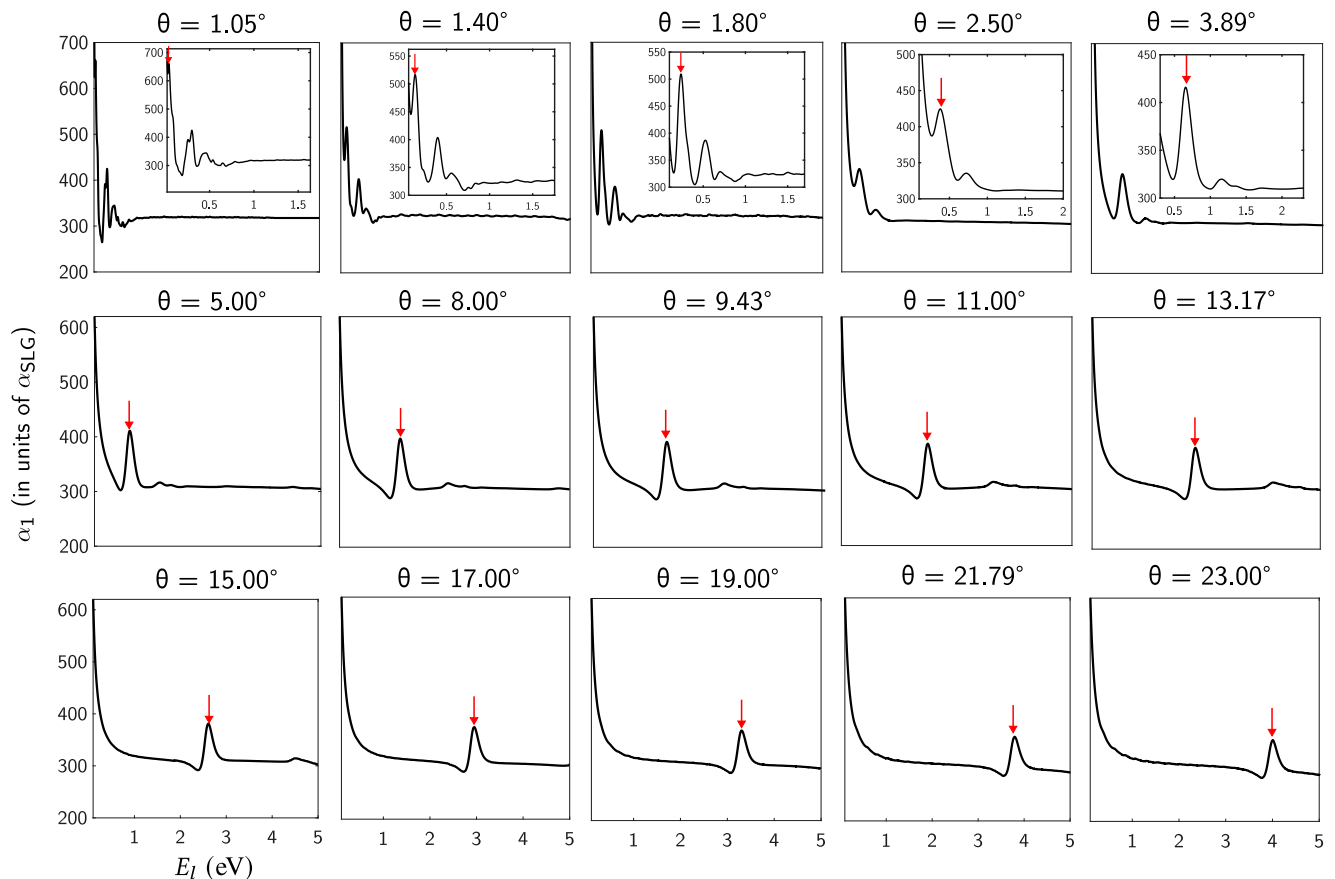


FIG. 3. The one-photon absorption coefficient α_1 as a function of the incoming excitation energy E_l as the twist angle θ is increased from 1.05° to 23° . The inset of the figure shows the details of the resonance feature. The red arrows mark the location of resonant absorption peak.

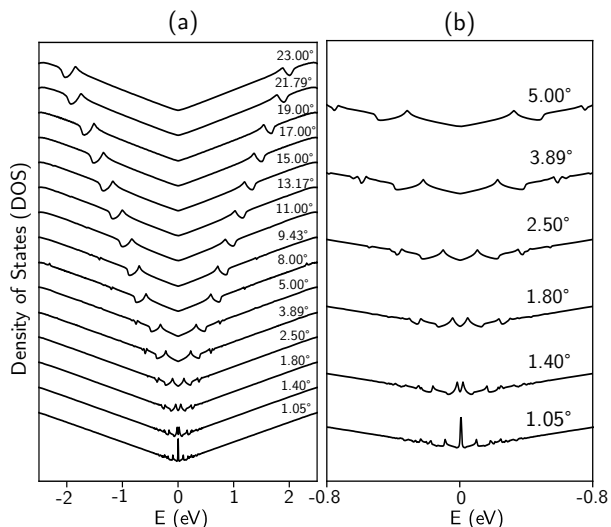


FIG. 4. The DOS of TBLG with various twist angles θ for (a) wide and (b) narrow energy range.

where, $I = \epsilon_0 c \omega^2 A^2 / 2$ is the incident radiation intensity (in W/m^2) and the factor 2 accounts for the electron-

spin degeneracy [81]. It is usually challenging to calculate accurate numerical values from the MPA transition probabilities because they require the knowledge of the interaction Hamiltonian matrix elements among *all* of the eigenstates as, well as summations over *all* of its energy bands. Additionally, the knowledge of all the energy eigenvalues as functions of the wave vector \mathbf{k} through the first Brillouin zone is also needed [41].

In this paper we focus on the single- and two-photon absorption processes for TBLG by considering its full band structure while involving all the possible transitions between the occupied and unoccupied states. FIG. 1 (a) represents the schematic of the OPA process, where an electron makes a transition from a valence band to a conduction band state on absorption of a single photon of frequency ω . The corresponding Feynman diagram is shown in FIG. 1 (b). The transition probability rate for this process is given by

$$W_1 = \frac{2\pi}{\hbar} \int_{\mathbf{k}} |\langle f | H_{eR} | i \rangle|^2 \delta(E_f - E_i - \hbar\omega) \frac{d^3\mathbf{k}}{(2\pi)^3} \quad (4)$$

and the one-photon absorption coefficient is

$$\alpha_1 = \frac{2\hbar\omega W_1}{I} \quad (5)$$

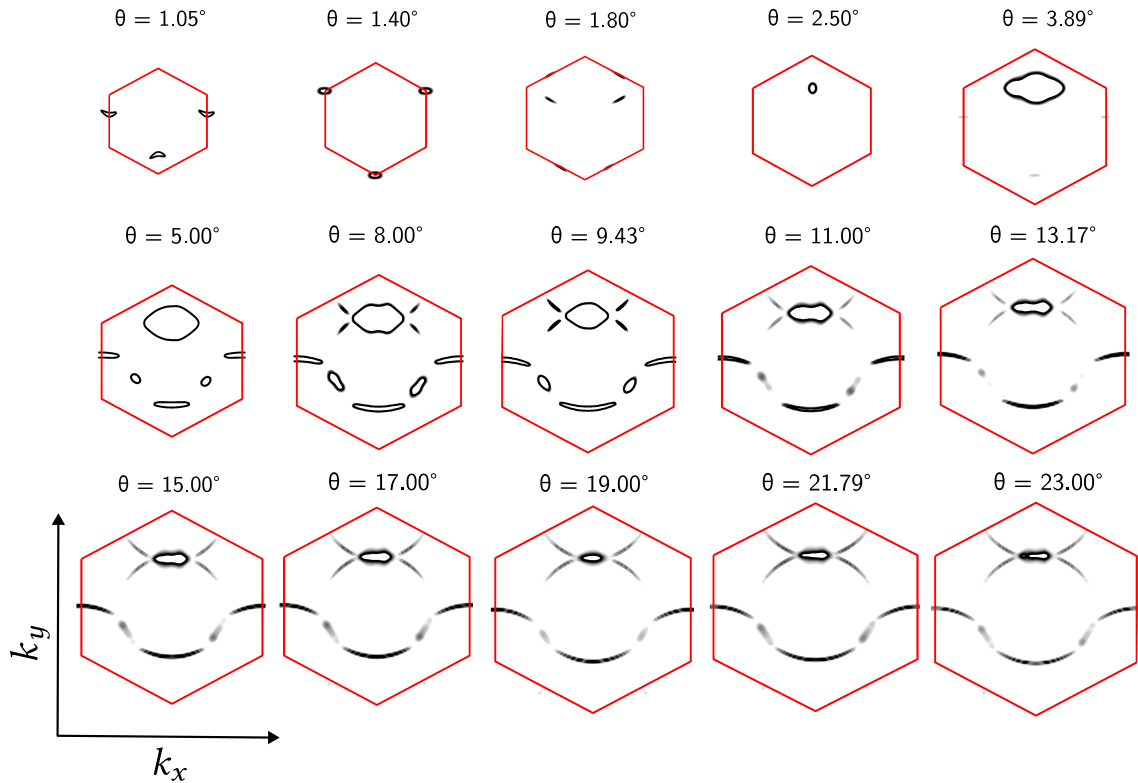


FIG. 5. The dark regions mark the location of the wavevectors giving the dominant contribution to the one-photon absorption coefficient α_1 at the excitation energy E_o indicated by the red arrows in FIG. 3. The red hexagon outlines the MBZ.

TPA is an interband transition wherein two photons, each of energy $\hbar\omega$ are absorbed simultaneously, thereby creating an electron in the conduction band and a hole in the valence band [52]. Both the photons can either be absorbed simultaneously or in a step-wise manner. From FIG. 1 we see that the leading contribution to the matrix element for the first process to TPA is of the first-order in the interaction term. Both the photons are annihilated at the same point, which makes this process analogous to OPA. In contrast, the leading contributions of the second possible process are second-order in the interaction term. The major difference between both the processes is the lack of the presence of an intermediate state in the absorption involving the annihilation of both photons simultaneously [82].

FIG. 1 (c) shows the schematic of an experimental setup for photon absorption. We have a laser source that emits photons of frequency ω , a polarizer that controls the polarization direction of the incident light, the material system under consideration (TBLG in our case), and the photon-detector. The transmitted signals are measured using the lock-in technique [83–85] which detects small AC signals obscured by a noisy environment. The photons produced by the laser source pass through the polarizer and interact with the electronic subsystem of the material via the light-matter interaction Hamiltonian H_{eR} .

From first-order perturbation theory, the transition

amplitude for the simultaneous absorption of two photons, where there are no intermediate states, is given as [41]:

$$\mathcal{T}_{fi}^1 = \langle \psi_f | H_{eR} | \psi_i \rangle \quad (6)$$

while for the second process which involves the intermediate states is

$$\mathcal{T}_{fi}^2 = \sum_m \frac{\langle \psi_f | H_{eR} | \psi_m \rangle \langle \psi_m | H_{eR} | \psi_i \rangle}{E_i(\mathbf{k}) + \hbar\omega - E_m(\mathbf{k}) - i\gamma} \quad (7)$$

and, hence the total transition probability rate for the two-photon absorption is given by

$$W_2 = \frac{2\pi}{\hbar} \int_{\mathbf{k}} \sum_{i,f} |\mathcal{T}_{fi}^1 + \mathcal{T}_{fi}^2|^2 \delta(E_i - E_f - 2\hbar\omega) \frac{d^3\mathbf{k}}{(2\pi)^3} \quad (8)$$

The expression for the TPA absorption coefficient is

$$\alpha_2 = \frac{4W_2\hbar\omega}{I^2} \quad (9)$$

The domain of integration over \mathbf{k} includes the entire Brillouin zone (BZ) of the crystalline material system under study and the summation over i and f includes all the initial and final states of transition. $|\psi_i\rangle$ and $|\psi_f\rangle$ represent the initial and final state of the transition with energies E_i and E_f , respectively. The summation over $|m\rangle$ and

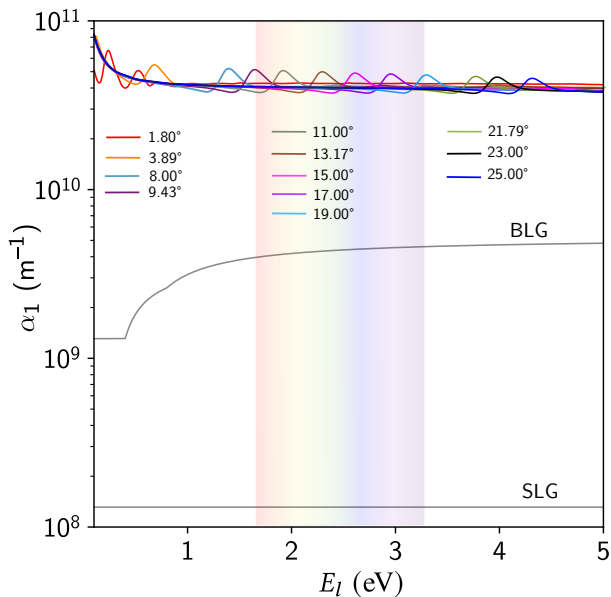


FIG. 6. The one-photon absorption coefficient α_1 as a function of E_l for SLG, BLG and TBLG. The colored region marks the visible energy range.

$|n\rangle$ (with energies E_m and E_n) is taken over all the possible intermediate states. γ is the broadening parameter which is taken to be a fixed fraction $\approx \frac{1}{20}th$ of the laser energy for all the considered transitions due to the unavailability of its dependence on the laser energy in the literature. In our calculations, in order to evaluate the quantities from Eqs. 6- 8, for a given pair of initial and final state of transition, we take the summation over all the possible intermediate states, represented by the index m with all the bands converged up to 10^{-2} eV within a specific energy window. The cut offs for the minimum and maximum energies of this energy window depend on the value of the incoming laser energy E_l such that the energy gap is far beyond E_l . Under the assumption that the photon wave vector is negligible as compared to the electronic wave vector (dipole approximation) [86], the vector potential \mathbf{A} can be separated from the expectation value. The term $\langle \psi_f | H_{eR} | \psi_i \rangle$ appearing in the numerator of Eq. 7 will be generically referred to as the "optical matrix element" in the subsequent discussion.

In the literature, there have been several experimental techniques like nonlinear transmission (NLT) [87–92], nonlinear luminescence (NLL) [93, 94], nonlinear photoconductivity (NLP) [95, 96], or the Z-scan technique [97, 98] to determine the value of the OPA and TPA absorption coefficients. In the next section, we shall discuss the continuum model of TBLG [27] and its interaction with photons.

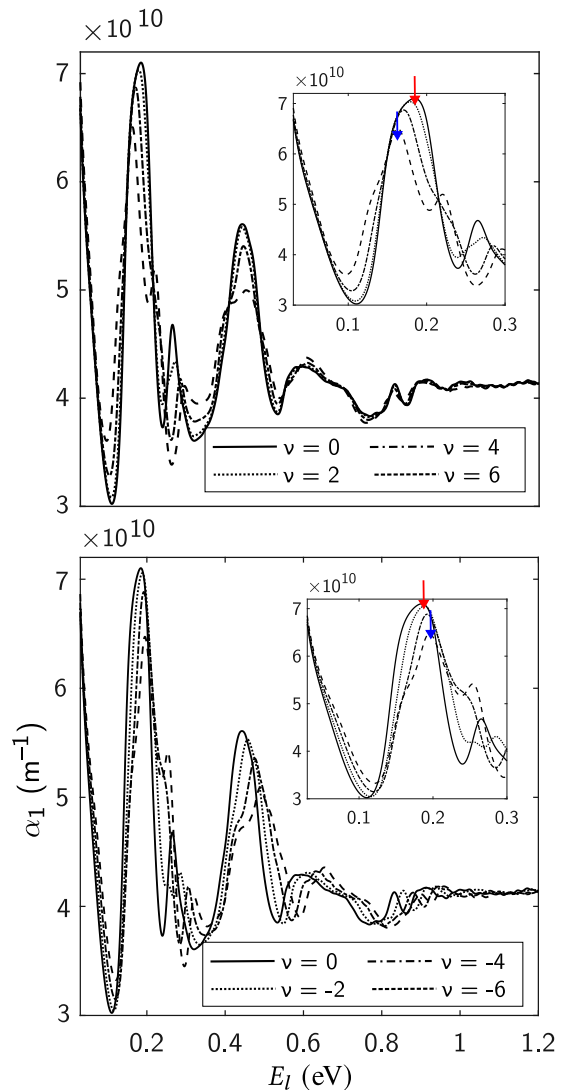


FIG. 7. The one-photon absorption coefficient α_1 as a function of E_l for twist angle $\theta = 1.54^\circ$ for (a) electron and (b) hole doping, respectively.

III. THE MODEL HAMILTONIAN

FIG. 2 (a) represents a two-dimensional (top) view of TBLG where the two graphene layers are rotated by a misorientation angle θ w.r.t. each other. The black hexagon marks the moiré unit cell with the AA and AB regions indicated. The corresponding rotated Brillouin zones are depicted in FIG. 2 (b), where the vectors \mathbf{q}_b , \mathbf{q}_{tr} , and \mathbf{q}_{tl} , respectively, denote the Dirac points of the top and bottom layers. They stand in for the momentum transfer associated with the three inter-layer hopping processes marked by the black arrows in the MBZ. FIG. 2 (c) and (d) shows the band structure along the high-symmetry path of MBZ. The number of bands in a given energy range increases as the twist angle θ is reduced [21], accounting for an increased number of transitions between the valence and conduction bands. By

turning on the light-matter interaction, the operator ∇ is replaced by $\nabla \rightarrow \nabla + ie\mathbf{A}/\hbar$ [99–101], where \mathbf{A} is the vector potential of the incident light with a magnitude A and polarization vector \mathbf{e} . The real-space model

$$H_{\text{TBLG}} = \sum_{l=1,2} \int d^2\mathbf{r} \hat{\Psi}_l^\dagger(\mathbf{r}) [v_F \boldsymbol{\sigma}_l \cdot (-i\hbar\nabla + e\mathbf{A}) + V_H(\mathbf{r})] \hat{\Psi}_l(\mathbf{r}) + \int d^2\mathbf{r} [\hat{\Psi}_1^\dagger(\mathbf{r}) T'(\mathbf{r}) \hat{\Psi}_2(\mathbf{r}) + \text{h.c.}] \quad (10)$$

where, $\hat{\Psi}_l(\mathbf{r})$ is the two-component field-operator corresponding to the layer l , v_F is the Fermi velocity in graphene and $\boldsymbol{\sigma}_l = e^{i(-1)^l \sigma_z \theta/4} (\sigma_x, \sigma_y) e^{-i(-1)^l \sigma_z \theta/4}$ are the Pauli-matrices vector which account for the rotation of the individual graphene layer. On including the electron-electron interactions *via* self-consistent Hartree calculations [105–109], it is found that the electronic band structure of doped TBLG changes significantly. We employ the parametrization provided by Goodwin *et al.* [105], according to whom the doping and twist angle-dependent Hartree potential energy is described by $V_H(\mathbf{r}) \approx \mathcal{V}_\theta \sum_{j=1}^3 \cos(\mathbf{G}_j \cdot \mathbf{r})$ where, $\mathcal{V}_\theta = V(\theta) [\nu - \nu_o(\theta)]$. The quantity $\nu_o(\theta)$ represents the doping level at which the Hartree potential vanishes, $V(\theta)$ is a θ dependent energy parameter, ν is the filling factor, and \mathbf{G}_j denotes the reciprocal lattice vectors that are used to describe the out-of-plane coordinates of TBLG [67]. This equation has a form similar to the continuum model provided in Ref. [107]. The spatially dependent interlayer tunneling matrices $T'(\mathbf{r})$ appearing as off-diagonal elements in Eq. 10 forms a smooth moiré potential [27] of the form [103, 104, 110]

$$T'(\mathbf{r}) = \sum_{j=1}^3 e^{-i\mathbf{q}_j \cdot \mathbf{r}} T'_j \quad (11)$$

where, the T'_j matrices are given by [103, 104, 110]

$$T'_j = (w_o \sigma_o + iw_3 \sigma_z) + w_1 \left[\sigma_x \cos(\phi') + \sigma_y \sin(\phi') \right] \quad (12)$$

Here, $\phi' = 2\pi(j-1)/3$ and $\boldsymbol{\sigma}$ are the Pauli matrices. The w_o term contributes to the diagonal elements and represents the interlayer coupling between the A(B) sublattice of the top layer and the A(B) sublattice of the bottom layer. The w_1 term only contributes to the off-diagonal elements and is thus associated with the interlayer coupling between the A(B) sublattice of the top layer and B(A) sublattice of the bottom layer. w_3 is defined as the interlayer contact coupling and as shown by Kang *et al.* [104], it accounts for the dominant source of the non-negligible ph asymmetry in the model of Ref. [38]. Setting $w_o = w_1$, $w_3 = 0$ and keeping \mathbf{q}_j in the first shell recovers the tunneling matrices of the original BM continuum model [27]. A minor contribution arises from the gradient coupling λ which has therefore not been taken

Hamiltonian for TBLG incorporating the effects of corrugation, doping-dependent Hartree interactions and ph-asymmetry is [27, 67, 102–104],

into account for the purpose of our calculations. The corrugation effect substantially alters the electron band structure near the Γ point of the MBZ and can be included by setting $w_o \neq w_1$ in Eq. 12 [67, 111].

The interaction of photons with TBLG is discussed and derived in our previous work [112] where we had also demonstrated that the optimum model used to describe the absorption of TBLG is to include corrugation effects [67] in the continuum model of pristine TBLG [27]. A similar demonstration is provided in Appendix B for an arbitrary twist angle.

IV. RESULTS

A. The one-photon absorption coefficient as a function of the incoming laser energy

In FIG. 3, we plot α_1 as a function of excitation energy E_l for various twist angles ranging from 1.05° to 23° by considering all the possible transitions from the occupied to the empty states. α_1 is plotted in units of

$$\frac{e^2}{2\hbar c \epsilon_o d} \quad (13)$$

which is the OPA absorption coefficient for single-layer graphene (SLG) under the linear band approximation, where d is the sample thickness. Through our calculations, we find that for higher twist angles, like $\theta \gtrsim 3^\circ$, only one major absorption peak is present with its location associated with the van Hove singularity. As the twist angle decreases, apart from the major resonant absorption peak, we see the presence of other minor peaks (refer to the inset of FIG. 3) associated with the interaction of other peaks originating in the DOS (plotted in FIG. 4). The energy value of the major absorption peak (marked by red arrows in FIG. 3) continuously decreases as the twist angle is reduced, accompanied by additional peaks in low energy regime, *i.e.*, $E_l \lesssim 1$ eV. For instance, the resonant feature in α_1 for $\theta \sim 2.5^\circ$ occurs at ~ 0.38 eV. This energy value increases to ~ 0.86 eV and ~ 3 eV as θ is increased to $\sim 5^\circ$ and $\sim 17^\circ$, respectively. The location of the major peak is indicated by the red arrows in FIG. 3. In FIG. 4, we provide the DOS over the entire first MBZ for various twist angles and we in-

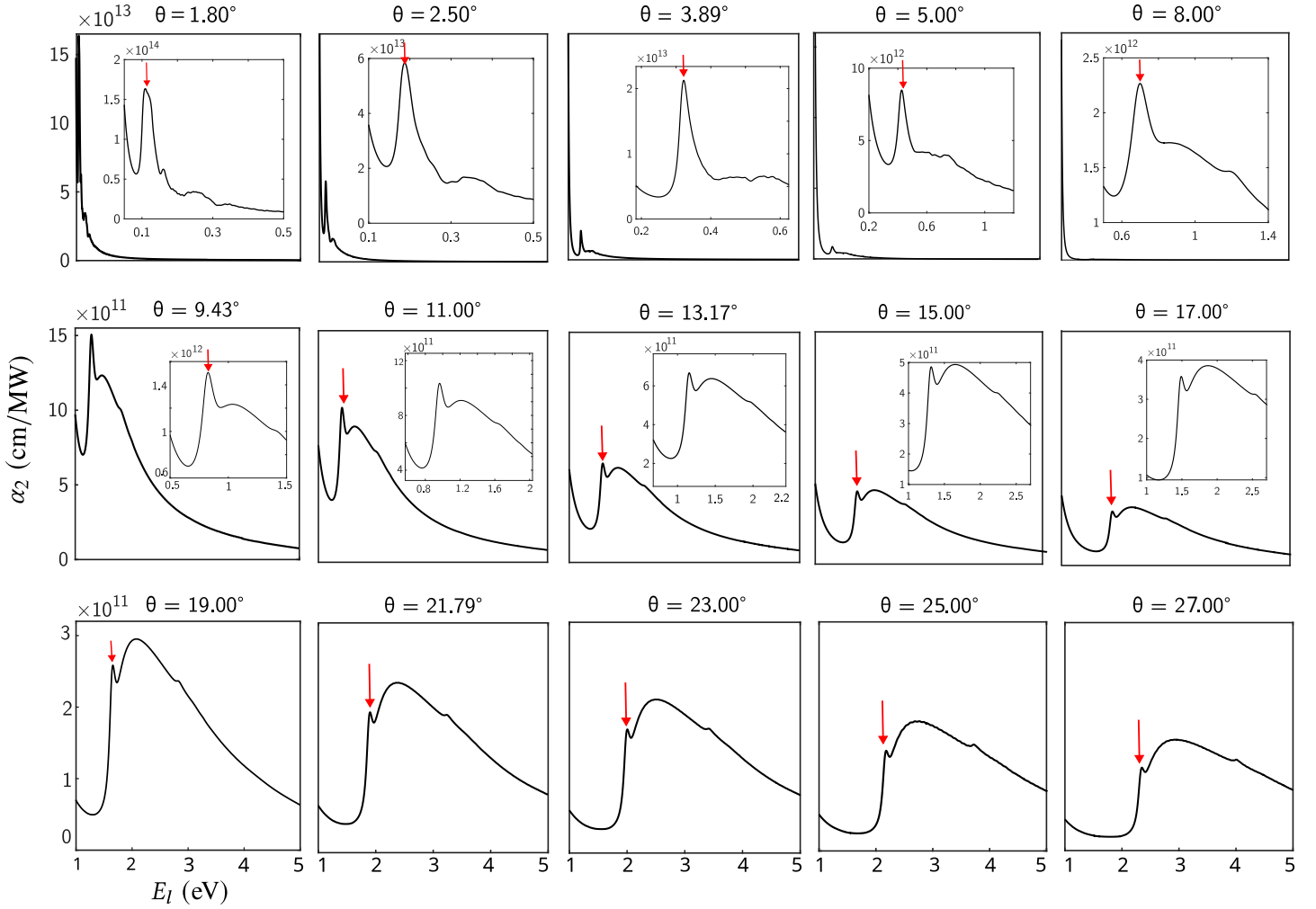


FIG. 8. The two-photon absorption coefficient α_2 as a function of the incoming excitation energy E_l . The inset of the figure shows the details of the resonance features. The red arrows mark the location of the resonant absorption peaks.

fer that the peak energy of the major absorption peak is associated with the van Hove singularities of TBLG.

To identify the region in the MBZ which gives the dominant contribution to α_1 in FIG. 3, we provide the contour plot for α_1 as function of k_x and k_y in the entire first MBZ of TBLG in FIG. 5. The excitation energies at which the contour is plotted is marked by red arrows in FIG. 3. For higher twist angles, the location of the wavevectors giving the dominant contribution to OPA saturates. However, as the twist angle reduces, these wavevectors begin confining in a certain region of the MBZ. *E.g.* for $\theta \lesssim 2.5^\circ$, the location of the wavevectors start shifting towards the K point of the MBZ. At $\theta \sim 1.4^\circ$, the contribution arises exactly from the K point. Further lowering the twist angle shifts this region away from the K - to the M -point.

From Fig. 6 we see that for $E_l \lesssim 5$ eV, α_1 displays an enhancement by ~ 2 and ~ 1 orders of magnitude when compared to SLG and BLG, respectively. The increase in the order of magnitude rises continuously as the twist angle is reduced. By changing the twist angle, the resonance feature exhibited by α_1 can be tuned to different

excitation energies. *For instance*, for $\theta \lesssim 9^\circ$, the infrared region gives the maxima of α_1 , whereas for higher twist angles, the resonant feature progressively scans the visible excitation energies.

The parameterized form of the doping and twist angle-dependent Hartree potential energy provided by Goodwin *et al.* [105] is discussed in Sec. III. We study the effect of the doping level on α_1 and the results for electron and hole doping are presented in Figs. 7 (a) and (b), respectively, for an arbitrary twist angle, $\theta \sim 1.54^\circ$. The inset of figure shows the zoom-in for low energy values. For both cases, we find that the behavior of α_1 vs. E_l remains essentially unaltered but with a minor red-shift of its resonant peaks. The red arrow indicates the energy value of ~ 0.185 eV for undoped TBLG. This value changes to ~ 0.16 eV and ~ 0.2 eV (indicated by the blue arrows in FIG. 7) for higher electron and hole filling factors, respectively. Therefore, this spectroscopic method may provide an experimental means to establish a relatively undoped sample for an arbitrary twist angle.

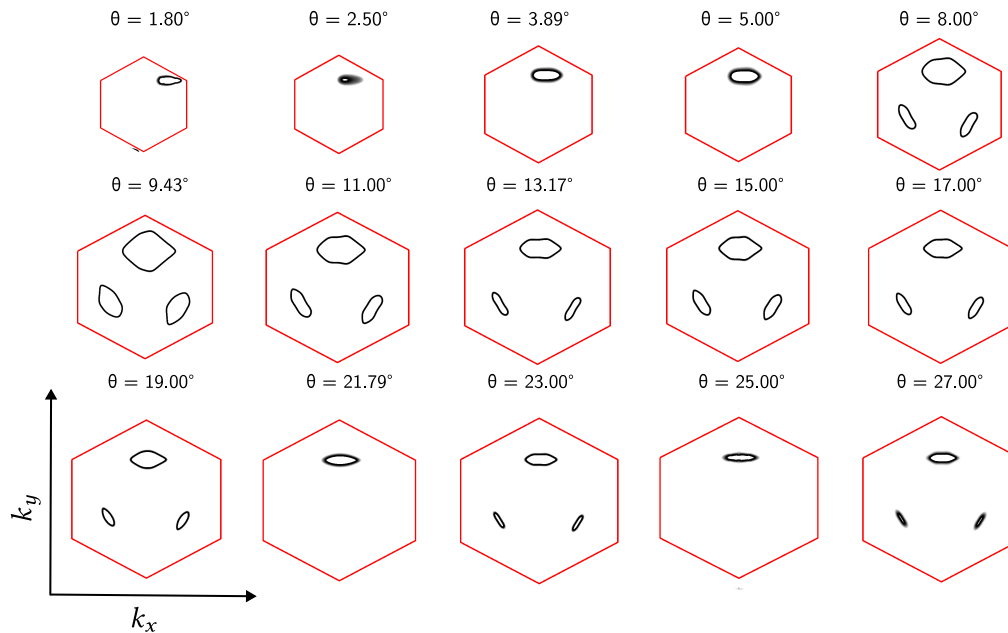


FIG. 9. The dark regions mark the locations of the wavevectors giving the dominant contribution to the two-photon absorption coefficient α_2 at the excitation energy E_o indicated by red arrows in FIG. 8. The red hexagon outlines the MBZ.

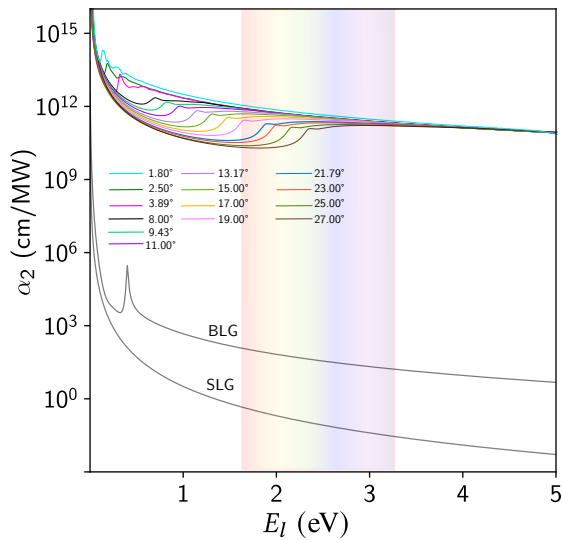


FIG. 10. The two-photon absorption coefficient α_2 as a function of E_l for SLG, BLG and TBLG for various twist angles mentioned in the legend. The colored region marks the visible energy range.

B. The two-photon absorption coefficient as a function of the incoming laser energy

By considering both the possible processes presented in FIG. 1, we consider the behavior of α_2 discussed in Sec. II *vs.* E_l in FIG. 8 for various θ . Our results show that α_2 is characterized by a resonant peak at twice the wavelength or half the energy at which the resonance occurs for the one photon case. *For e.g.*, for $\theta \sim 5^\circ$, FIG. 8 shows that

the resonant feature for α_2 occurs at $E_o \sim 0.42$ eV, which is exactly half the value obtained for α_1 as shown by the red arrow in FIG. 3. Similarly, for $\theta \sim 2.5^\circ$, α_2 has a resonant peak at ~ 0.19 eV, while for α_1 it appears at ~ 0.38 eV.

Similar to the OPA process, in order to identify the location of wavevectors that give the major contribution to the resonant peak in α_2 *vs.* E_l , we present the contour plot of α_2 as a function of k_x and k_y in the entire first MBZ in FIG. 9 and mark the location of the dominant wavevectors in the dark color. We see that their location stabilizes for higher twist angles like $\theta \gtrsim 8^\circ$ and starts shifting towards the K point as the twist angle is further reduced.

In FIG. 10, we provide a clear distinction in the behavior of TPA coefficient for SLG, BLG [113] and TBLG for various twist angles. Irrespective of the twist angle, the magnitude of TPA coefficient shows a giant enhancement by ~ 9 and ~ 11 orders for the visible range of excitation energies, compared to BLG and SLG, respectively. For comparison we provide the values of α_2 for a selection of 2D materials in Table I. This giant enhancement in the TPA absorption TBLG can be explained as follows. For reference we shall consider the case of SLG or BLG, where the density of states (DOS) in the optical energy range are within the same order of magnitude and arise only from a single- (two-) band pair for SLG (BLG). However, if we look at the band structure for TBLG as shown in Fig. 2(c-d), there are a multiplicity of bands in the same optical energy range, and thus a correspondingly greater contribution to the DOS. It also helps that these bands have a lower slope than the those of SLG/BLG in the same energy range. Further, as the

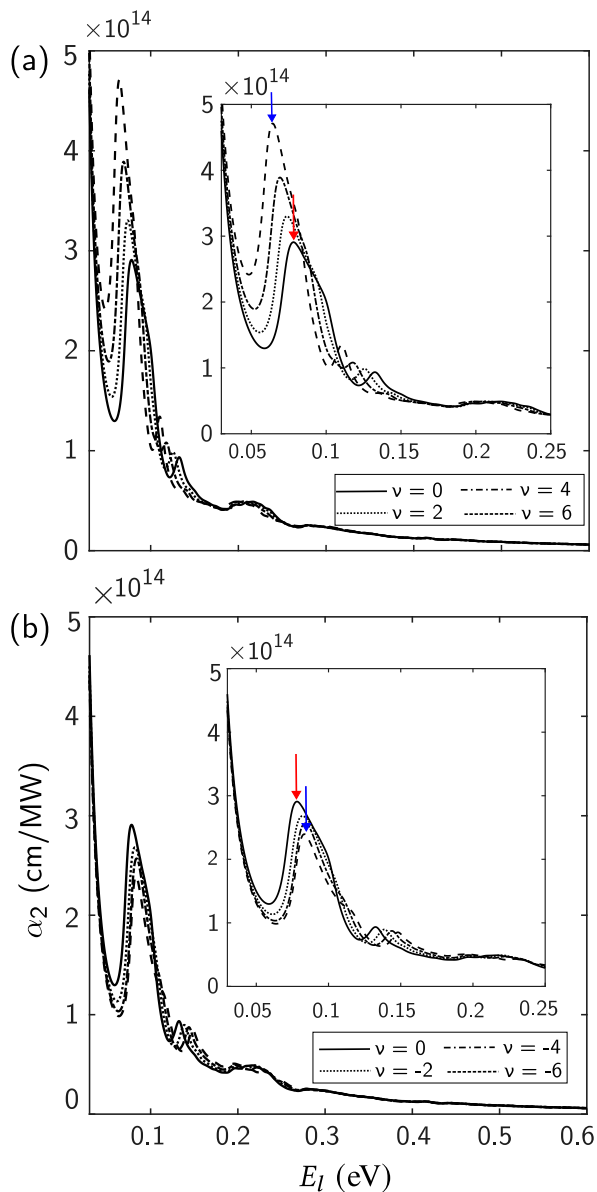


FIG. 11. The two-photon absorption coefficient α_2 as a function of E_l for a twist angle $\theta = 1.54^\circ$ for (a) electron and (b) hole doping, respectively.

twist angle is reduced, a larger number of bands confine in a given energy range, which further increases the number of states available for transition. Hence as the twist angle is reduced, the value of $\alpha_{i=1,2}$ continuously rises. From Fig. 10 we see that the location of resonant peak is highly dependent on the twist angle and scans different energy region as the twist angle is varied. The resonant feature of α_2 for $\theta \gtrsim 19^\circ$ is obtained in the visible range, whereas, for smaller angles, it is obtained in the infra-red region. Compared to BLG, the magnitude of the resonant peak is greatly enhanced by ~ 9 orders for $\theta = 1.8^\circ$ and this factor increases continuously as θ decreases.

The effect of electron and hole doping on the behavior of α_2 is shown in FIG. 11 (a) and (b), respectively.

| Material | $\hbar\omega$ (eV) | α_2 (cm/MW) |
|-------------------------|--------------------|--------------------|
| WS ₂ [116] | 1.54 | 3.7×10^2 |
| MoS ₂ [117] | 1.2 | 7.62 |
| MoSe ₂ [118] | 1.2 | 1.8 |
| MoS ₂ [119] | 2.3 | 5×10^{-4} |
| WSe ₂ [120] | 1.16 | 7.29 |

TABLE I. Values of TPA coefficients for few 2d materials at different laser energies.

We find that on doping there is a minor red-shift of the resonant peaks in α_2 vs E_l . For electron doping, the peaks shift to the left, while for the case of hole doping, the peaks make a transition towards the right. The red arrows mark the energy of the resonant peak for an undoped TBLG.

In order to study the effect of the polarization direction of the two driving photons on α_2 , we define the polarization directions of the two photons as θ_{P1} and θ_{P2} , respectively, measured relative to an unrotated graphene sheet (refer FIG. 12 (a) for the parallel and cross-polarized configurations). Firstly, we vary both θ_{P1} and θ_{P2} simultaneously in-phase and secondly, we keep θ_{P1} fixed and $\theta_{P2} = \theta_{P1} + \phi$, where we scan ϕ from 0° to 90° . For the former configuration, we observe that α_2 is isotropic in nature. However, for the latter, our results show that when $\phi = 90^\circ$, *i.e.*, both the photons are cross-polarized *w.r.t* each other, α_2 attains a minimum value. In contrast, α_2 attains a maxima for the parallel-polarized configuration, *i.e.*, when $\theta_{P1} = \theta_{P2}$. In FIG. 12 (b), we represent the result for a sample twist angle $\theta \sim 3^\circ$ where we see that as ϕ is increased from 0° to 90° , the value of α_2 keeps on decreasing. This is due to *interference effects* [112, 114, 115] mediated by the optical matrix elements appearing in Eq. 8. The area under the curve for α_2 vs. E_l for $\theta \sim 3^\circ, 4^\circ$ is plotted in FIG. 12 (c) and displays an isotropic nature when the polarization direction of the two photons are varied simultaneously and in phase. However, when they are rotated independently, we see that the area under curve exhibits an anisotropic behavior, giving a maxima at $\phi = 0^\circ$ and minima at $\phi = 90^\circ$.

V. CONCLUSION

In summary, our research delved the absorption properties of twisted bilayer graphene (TBLG), with a specific focus on both single- and two-photon absorption processes involving different stacking configurations and polarization orientations. We employed the effective continuum model for our analysis. Our findings revealed distinctive features for the absorption coefficient α_1 , which exhibited a series of absorption peaks corresponding to the van Hove singularities within the band structure. For

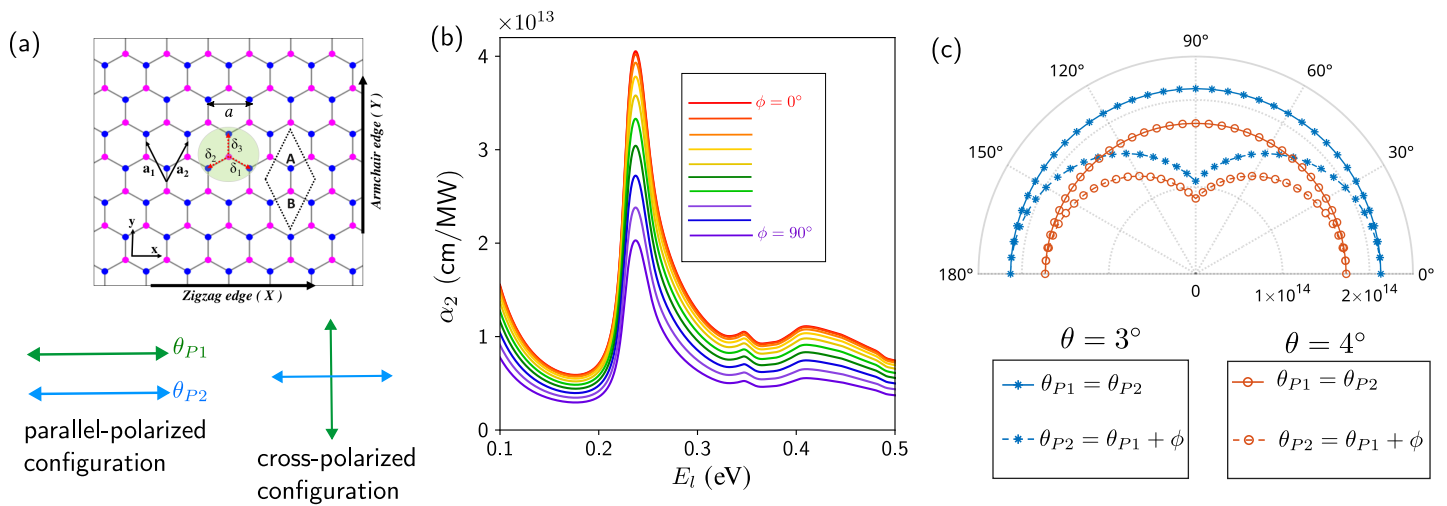


FIG. 12. (a) The real-space lattice structure of single-layer graphene (SLG). The green and blue double-headed arrows mark the polarization direction of the two photons, θ_{P1} and θ_{P2} , respectively, involved in TPA. (b) The variation of the two-photon absorption coefficient α_2 as a function of the incoming laser energy E_l where $\theta_{P2} = \theta_{P1} + \phi$ for $\theta \sim 3^\circ$. ϕ is increased from 0° to 90° in steps of 10° . (c) The area under the curve for α_2 as a function of the incoming energy E_l for $\theta \sim 3^\circ$ and 4° . The polar axis marks ϕ while the radial axis represents area under the curve for α_2 vs E_l .

two-photon absorption in TBLG, we found the presence of a resonance peak for α_2 at nominally half the energy of the single-photon case. Compared to AB bilayer graphene (BLG), α_2 displayed a significant increase of 9 orders of magnitude in the visible energy range, with an even more substantial increase in the infrared energy range. Furthermore, as we varied the twist angle, the resonant feature associated with α_1 and α_2 shifted from the infrared to visible excitation energies. We also explored the impact of doping on the absorption coefficient and noted that, as the level of doping increased, the behavior of α_1 and α_2 with respect to the excitation energy E_l remained consistent, accompanied by a minor redshift of their resonant peaks. Our findings suggest that this spectroscopic technique can serve as an experimental method for determining the relative rotation angle of TBLG and identifying samples with relatively low doping levels. In addition to these observations, we investigated the behavior of α_2 under various polarization configurations. Our analysis revealed that α_2 exhibited isotropic and anisotropic behaviors when the polarization directions of the two photons were altered either simultaneously or independently, respectively.

Our work also represents, to the best of our knowledge [121], the first calculation of the absorption coefficients of TBLG by explicitly involving all the possible transitions from the occupied to empty states. It would be interesting to experimentally determine the value of the absorption coefficients for TBLG with the use of Quantum Cascade lasers [66, 122–125] which are capable of emitting mid-infrared light. By varying the twist angle, the resonance in the absorption coefficients of TBLG can be tuned to different energy regimes, making TBLG an interesting prospect for the engineering of solar pan-

els.

VI. ACKNOWLEDGMENT

Disha Arora acknowledges The Department of Science and Technology, Government of India, for supporting this work *via* the INSPIRE fellowship scheme. Deepanshu Aggarwal is supported by the UGC, Government of India Fellowship.

Appendix A: Current density operator in twisted bilayer graphene

As mentioned in the Sec. II of the main text, an alternative approach to evaluating the absorption coefficients is by first calculating the macroscopic current operator \mathbf{j} [75] which is determined by calculating the product of the velocity operator \mathbf{v} and density matrix ρ . In the tight-binding formalism [126] the Hamiltonian is constructed from the Bloch sums that spans the different sublattices (say N) constituting the lattice. In the basis set of these Bloch sums, the density matrix ρ , and hence the operator \mathbf{j} is of $N \times N$ dimensions. However, in moiré systems like TBLG [21], the effective continuum Hamiltonian [27] acts on the Bloch states that themselves constitute an infinite basis set. In reciprocal space, the Hamiltonian operator will thus consist of infinite matrix elements. In order to obtain a matrix of finite size, the number of reciprocal lattice vectors are truncated such that all the bands in a specific energy window (chosen well beyond the incoming laser energy) are converged to a predetermined tolerance. In this section we show the

evaluation of the current operator for TBLG by employ-

ing the low energy effective continuum model [27].

The real-space Hamiltonian of TBLG is given as

$$H_{\text{TBLG}} = \sum_{\ell=1,2} \int d^2\mathbf{r} \hat{\Psi}^{(\ell)\dagger}(\mathbf{r}) \left[v_F \boldsymbol{\sigma}_\ell \cdot (-i\hbar \nabla + e\mathbf{A}(\mathbf{r})) + V_H(\mathbf{r}) \right] \hat{\Psi}^{(\ell)}(\mathbf{r}) + \int d^2\mathbf{r} \left[\hat{\Psi}^{(1)\dagger}(\mathbf{r}) T'^{\dagger}(\mathbf{r}) \hat{\Psi}^{(2)}(\mathbf{r}) + \text{h.c.} \right] \quad (\text{A1})$$

The description of each term is provided in Sec. III of the main text. In order to calculate the current density operator in TBLG, we first separate out the unperturbed Hamiltonian and the perturbation due to light-matter in-

teraction. In the second quantized form, the unperturbed H_{TBLG}^0 and perturbed H_{TBLG}^1 expressions of the Hamiltonian in Eq. A1 are

$$H_{\text{TBLG}}^0 = \sum_{\ell=1,2} \int d^2\mathbf{r} \hat{\Psi}^{(\ell)\dagger}(\mathbf{r}) \left[-i\hbar v_F \boldsymbol{\sigma}^{(\ell)} \cdot \nabla + V_H(\mathbf{r}) \right] \hat{\Psi}^{(\ell)}(\mathbf{r}) + \int d^2\mathbf{r} \left[\hat{\Psi}^{(1)\dagger}(\mathbf{r}) T'^{\dagger}(\mathbf{r}) \hat{\Psi}^{(2)}(\mathbf{r}) + \text{h.c.} \right] \quad (\text{A2})$$

$$H_1^{\text{TBLG}} = \sum_{\ell=1,2} \int d^2\mathbf{r} \hat{\Psi}^{(\ell)\dagger}(\mathbf{r}) \left[e v_F \boldsymbol{\sigma}^{(\ell)} \cdot \mathbf{A}(\mathbf{r}) \right] \hat{\Psi}^{(\ell)}(\mathbf{r}) \quad (\text{A3})$$

where the Pauli-matrices $\boldsymbol{\sigma}^{(\ell)}$ account for the rotation of the layers. The perturbed Hamiltonian H_{TBLG}^1 can equivalently be represented using the complete set of the Bloch states of the unperturbed Hamiltonian H_{TBLG}^0 by writing the field operators as

$$\hat{\Psi}^{(\ell)}(\mathbf{r}) = \sum_{n,\mathbf{k}} \Psi_{n\mathbf{k}}^{(\ell)}(\mathbf{r}) \hat{c}_{n\mathbf{k}}^{(\ell)} \quad \text{and} \quad \hat{\Psi}^{(\ell)\dagger}(\mathbf{r}) = \sum_{m,\mathbf{k}'} \Psi_{m\mathbf{k}'}^{(\ell)\dagger}(\mathbf{r}) \hat{c}_{m\mathbf{k}'}^{(\ell)\dagger} \quad (\text{A4})$$

where $\Psi_{n\mathbf{k}}^{(\ell)}(\mathbf{r})$ is the Bloch function contributed by layer- ℓ corresponding to the band index n and the Bloch wave-vector \mathbf{k} , and $\hat{c}_{n\mathbf{k}}^{(\ell)\dagger}$ ($\hat{c}_{n\mathbf{k}}^{(\ell)}$) are the creation (annihilation) operator corresponding to layer ℓ , band index n and momentum \mathbf{k} . In general, the representation of the perturbation H_{TBLG}^1 is not diagonal and is written as

$$H_{\text{TBLG}}^1 = e v_F \sum_{\ell=1,2} \sum_{n,\mathbf{k}} \sum_{m,\mathbf{k}'} \hat{c}_{m\mathbf{k}'}^{(\ell)\dagger} \int d^2\mathbf{r} \Psi_{m\mathbf{k}'}^{(\ell)\dagger}(\mathbf{r}) \left[\boldsymbol{\sigma}^{(\ell)} \cdot \mathbf{A} \right] \Psi_{n\mathbf{k}}^{(\ell)}(\mathbf{r}) \hat{c}_{n\mathbf{k}}^{(\ell)} \quad (\text{A5})$$

Restricting the reciprocal lattice vector $\mathbf{G} = 0, \mathbf{G}_1, -\mathbf{G}_1 - \mathbf{G}_2$, we get the 8×8 matrix representation of perturbed Hamiltonian as

$$\frac{H_1^{\text{TBLG}}}{e v_F} = \begin{bmatrix} \boldsymbol{\sigma}_{\theta/2} \cdot \mathbf{A} & 0 & 0 & 0 \\ 0 & \boldsymbol{\sigma}_{-\theta/2} \cdot \mathbf{A} & 0 & 0 \\ 0 & 0 & \boldsymbol{\sigma}_{-\theta/2} \cdot \mathbf{A} & 0 \\ 0 & 0 & 0 & \boldsymbol{\sigma}_{-\theta/2} \cdot \mathbf{A} \end{bmatrix} \quad (\text{A6})$$

The current density operator [76, 127, 128] in the second-quantized formalism is given as

$$\mathbf{j}(\mathbf{r}) = -e \left[\Psi_1^\dagger(\mathbf{r}) \quad \Psi_2^\dagger(\mathbf{r}) \right] \mathbf{v} \begin{bmatrix} \Psi_1(\mathbf{r}) \\ \Psi_2(\mathbf{r}) \end{bmatrix} \quad (\text{A7})$$

where, \mathbf{v} is the velocity operator defined as $= \frac{i}{\hbar} [H, r]$ [129] is given by

$$\frac{\mathbf{v}}{(i/\hbar)} = \begin{bmatrix} [h_1(-\theta/2) + V_H(\mathbf{r}), \mathbf{r}] & [T'^{\dagger}(\mathbf{r}), \mathbf{r}] \\ [T'(\mathbf{r}), \mathbf{r}] & [h_2(\theta/2) + V_H(\mathbf{r}), \mathbf{r}] \end{bmatrix} \quad (\text{A8})$$

Solving each term in the above matrix we get

$$\begin{aligned} [h_1(-\theta/2) + V_H(\mathbf{r}), \mathbf{r}] &= [h_1(-\theta/2), \mathbf{r}] + [V_H(\mathbf{r}), \mathbf{r}] \\ &= [h_1(-\theta/2), \mathbf{r}] \\ &\quad \text{and} \\ [h_1(-\theta/2) + V_H(\mathbf{r}), \mathbf{r}] &= [h_1(-\theta/2), \mathbf{r}] \end{aligned}$$

while $[T'(\mathbf{r}), \mathbf{r}] = [T'^{\dagger}(\mathbf{r}), \mathbf{r}] = 0$.

Therefore the velocity operator takes the form

$$\mathbf{v} = \frac{i}{\hbar} \begin{bmatrix} [h_1(-\theta/2), \mathbf{r}] & 0 \\ 0 & [h_2(\theta/2), \mathbf{r}] \end{bmatrix} \quad (\text{A9})$$

Using the commutation between the rotated Dirac

Hamiltonian and the position operator as

$$\begin{aligned} \frac{i}{\hbar}[h_1(-\theta/2), \mathbf{r}] &= v_F \boldsymbol{\sigma}_{\theta/2} \\ \frac{i}{\hbar}[h_2(-\theta/2), \mathbf{r}] &= v_F \boldsymbol{\sigma}_{-\theta/2} \end{aligned} \quad (\text{A10})$$

we can rewrite Eq. A9 as

$$\mathbf{v} = v_F \begin{bmatrix} \boldsymbol{\sigma}_{\theta/2} & 0 \\ 0 & \boldsymbol{\sigma}_{-\theta/2} \end{bmatrix} \quad (\text{A11})$$

Defining $|n\rangle = |\mathbf{k}, n\rangle$, for the Hamiltonian $H = H_0 + H_1$, leads to the von Neumann equation for the density matrix [76, 130]

$$i\hbar \frac{\partial}{\partial t} \rho_{mn} = [E_m(\mathbf{k}) - E_n(\mathbf{k})] \rho_{mn} + \sum_l [(H_1)_{ml} \rho_{ln} - \rho_{ml} (H_1)_{ln}] \quad (\text{A12})$$

The macroscopic current [75–77] is computed as

$$\mathbf{j}(t) = -e \sum_{mn} \mathbf{v}_{mn} \rho_{mn}(\mathbf{k}, t) \quad (\text{A13})$$

where $\mathbf{v}_{mn} = \langle m | \mathbf{v} | n \rangle$ are the matrix elements of the velocity operator. The current operator up to linear and second order in the electric field is given as [76, 77]

$$\begin{aligned} \mathbf{j}^1(t) &= -e \sum_{mn} \mathbf{v}_{mn} \rho_{mn}^{(1)}(\mathbf{k}, t) \text{ and} \\ \mathbf{j}^2(t) &= -e \sum_{mn} \mathbf{v}_{mn} \rho_{mn}^{(2)}(\mathbf{k}, t) \end{aligned} \quad (\text{A14})$$

In the above expression, $\rho_{mn}^{(1)}(\mathbf{k}, t)$ is the solution of the density matrix equation in the linear approximation with respect to the field and is given as [77]

$$\rho_{nm}^{(1)}(\mathbf{k}, t) = e \frac{(f_n^T(\mathbf{k}, \mu) - f_m^T(\mathbf{k}, \mu))(\mathbf{v} \cdot \mathbf{A})_{nm}}{E_n(\mathbf{k}) - E_m(\mathbf{k}) + \hbar\omega} e^{\eta t} \quad (\text{A15})$$

where, $V_{nm} = (\mathbf{v} \cdot \mathbf{A})_{nm}$ are the matrix elements of H_1 given in Eq. A6 in the Bloch basis and $\eta \rightarrow 0^+$ denotes the perturbation is turned on adiabatically at $t \rightarrow -\infty$. The zeroth order contribution to the density matrix $\rho_{nm}^{(0)} = \delta_{mn} f_n^T(\mathbf{k}, \mu)$ describes the occupation of the electrons in the ground state before the application of an external electric field to the system, which in the Bloch basis is the Fermi occupation functions denoted by $f^T(\mathbf{k}, \mu)$. The second order solution to Eq. A12 *i.e.* the term quadratic with respect to the field can be written as [76]

$$\begin{aligned} \rho_{nm}^{(2)}(\mathbf{k}, t) &= e^2 \sum_{l, \omega_1, \omega_2} \frac{(f_m^T(\mathbf{k}, \mu) - f_l^T(\mathbf{k}, \mu))(\mathbf{v} \cdot \mathbf{A})_{nl}(\mathbf{v} \cdot \mathbf{A})_{lm}}{(E_m(\mathbf{k}) - E_l(\mathbf{k}) + \hbar\omega_1 - i\hbar\eta)(E_n(\mathbf{k}) - E_m(\mathbf{k}) + \hbar(\omega_1 + \omega_2) - 2i\hbar\eta)} \\ &+ \frac{(f_n^T(\mathbf{k}, \mu) - f_l^T(\mathbf{k}, \mu))(\mathbf{v} \cdot \mathbf{A})_{nl}(\mathbf{v} \cdot \mathbf{A})_{lm}}{(E_n(\mathbf{k}) - E_l(\mathbf{k}) + \hbar\omega_1 - i\hbar\eta)(E_n(\mathbf{k}) - E_m(\mathbf{k}) + \hbar(\omega_1 + \omega_2) - 2i\hbar\eta)} e^{2\eta t} \end{aligned} \quad (\text{A16})$$

The absorption coefficient for incoming light with frequency ω is given as [74, 131, 132] $\alpha(\omega) \approx \frac{1}{\epsilon_0} \text{Im} [j(\omega)/A(\omega)]$. In Fig. 13, we have provided the plots for $\alpha_{i=1,2}$ and compared it with our results obtained from the methodology described in Sec. II. We see that both the approaches give identical behavior for $\alpha_{i=1,2}$. For illustration, we provide the expression for absorption coefficient using both formalisms for graphene in the linear band approximation. The transition probability from an initial valence band to a final conduction band for a single photon absorption is given as:

$$\begin{aligned} w_{i \rightarrow f} &= \frac{2\pi}{\hbar} \int_{\mathbf{k}} |\langle \Psi_{\mathbf{k},f} | H_P | \Psi_{\mathbf{k},i} \rangle|^2 \delta(E_f(\mathbf{k}) - E_i(\mathbf{k}) - \hbar\omega) \\ &\times [f_i^T(\mathbf{k}, \mu) \{1 - f_f^T(\mathbf{k}, \mu)\}] d^2\mathbf{k} \end{aligned} \quad (\text{A17})$$

where $f_i^T(\mathbf{k}, \mu)$ is the probability of the initial state i

being filled and $1 - f_f^T(\mathbf{k}, \mu)$ is the probability of the final state f being empty. At $T = 0$ K, the term $f_i^T(\mathbf{k}, \mu) [1 - f_f^T(\mathbf{k}, \mu)] = 1$. For finite temperature, we have the explicit form of the Fermi functions given as

$$f_i^T(\mathbf{k}, \mu) = \frac{1}{\exp\left(\frac{E_i(\mathbf{k}) - \mu}{k_B T}\right) + 1} \quad (\text{A18})$$

where T is the temperature and k_B is the Boltzmann constant. Considering the linear band dispersions for graphene as $E_s(\mathbf{k}) = s\hbar v_F k$ and $E_v(\mathbf{k})$, where s is the band index with value $s = +1(-1)$ for conduction

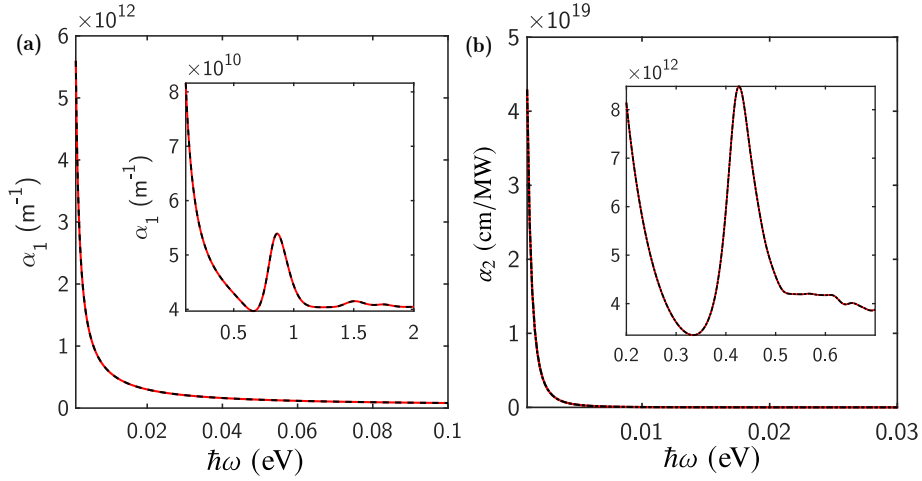


FIG. 13. Variation of α_1 and α_2 as a function of $\hbar\omega$ for $\theta \sim 5^\circ$. The red solid and black dashed lines represent the results of absorption coefficients evaluated by Eq. 3 in the main text and macroscopic current operator, respectively. The inset of Figs. shows the zoom-in for higher ω .

and valence band, respectively, we can rewrite $w_{i \rightarrow f}$ as

$$w_{i \rightarrow f} = \frac{1}{2\pi\hbar} \int_{\mathbf{k}} |\langle \Psi_{\mathbf{k},c} | H_P | \Psi_{\mathbf{k},v} \rangle|^2 \delta(2\hbar v_F k - \hbar\omega) \times \frac{\exp\left(\frac{\hbar v_F k - \mu}{k_B T}\right)}{\left[\exp\left(\frac{-\hbar v_F k - \mu}{k_B T}\right) + 1\right] \left[\exp\left(\frac{\hbar v_F k - \mu}{k_B T}\right) + 1\right]} d^2\mathbf{k}$$

On solving the integration over k , we get the first order transition probability

$$w_{i \rightarrow f} = \frac{A^2 e^2 \omega}{8\hbar^2} \frac{\exp\left(\frac{\frac{\hbar\omega}{2} - \mu}{k_B T}\right)}{\left[\exp\left(\frac{-\frac{\hbar\omega}{2} - \mu}{k_B T}\right) + 1\right] \left[\exp\left(\frac{\frac{\hbar\omega}{2} - \mu}{k_B T}\right) + 1\right]} \quad (\text{A19})$$

The photon absorption coefficient is given as $\alpha_1 = \frac{2\hbar\omega w_{i \rightarrow f}}{I d}$ which gives

$$\alpha_1 = \frac{e^2}{2\hbar c \epsilon_o} \frac{\exp\left(\frac{\frac{\hbar\omega}{2} - \mu}{k_B T}\right)}{\left[\exp\left(\frac{-\frac{\hbar\omega}{2} - \mu}{k_B T}\right) + 1\right] \left[\exp\left(\frac{\frac{\hbar\omega}{2} - \mu}{k_B T}\right) + 1\right]} \quad (\text{A20})$$

In order to find the expression of α_1 from the macroscopic current operator, the matrix elements of first order density operator are given as [76]

$$\rho_{s's'}^{(1)}(\omega) = \frac{e v_f [\boldsymbol{\sigma} \cdot \mathbf{A}]_{s's} (\rho_{ss} - \rho_{s's'})}{\hbar\omega - (E_{s'} - E_s)} \quad (\text{A21})$$

and the current operator as defined previously is given as

$$\mathbf{j}_{ss'}(\omega) = e \sum_{\mathbf{k}} \sum_{s's} \mathbf{v}_{s's} \rho_{ss'}(\omega) \quad (\text{A22})$$

where $v = v_F \boldsymbol{\sigma}$ is the velocity operator for graphene. Solving the above expression gives the absorption coefficient as

$$\alpha_1(\omega) = \frac{e^2}{2\hbar c \epsilon_o} \frac{\exp\left(\frac{\frac{\hbar\omega}{2} - \mu}{k_B T}\right) - \exp\left(\frac{-\frac{\hbar\omega}{2} - \mu}{k_B T}\right)}{\left[\exp\left(\frac{-\frac{\hbar\omega}{2} - \mu}{k_B T}\right) + 1\right] \left[\exp\left(\frac{\frac{\hbar\omega}{2} - \mu}{k_B T}\right) + 1\right]} \quad (\text{A23})$$

For a finite temperature and μ , Eq. A23 reduces to Eq. A20 for $\omega > \omega_o$.

Rewriting Eq. A17 for the DC response, we have

$$\rho_{nm}^{(2)}(\mathbf{k}, t) = e^2 \sum_{l, \omega_1, \omega_2} \frac{(f_m^T(\mathbf{k}, \mu) - f_l^T(\mathbf{k}, \mu)) (\mathbf{v} \cdot \mathbf{A})_{nl} (\mathbf{v} \cdot \mathbf{A})_{lm}}{(E_m(\mathbf{k}) - E_l(\mathbf{k}) + \hbar\omega_1 - i\hbar\eta) (E_n(\mathbf{k}) - E_m(\mathbf{k}) - 2i\hbar\eta)} + \frac{(f_n^T(\mathbf{k}, \mu) - f_l^T(\mathbf{k}, \mu)) (\mathbf{v} \cdot \mathbf{A})_{nl} (\mathbf{v} \cdot \mathbf{A})_{lm}}{(E_n(\mathbf{k}) - E_l(\mathbf{k}) + \hbar\omega_1 - i\hbar\eta) (E_n(\mathbf{k}) - E_m(\mathbf{k}) - 2i\hbar\eta)} e^{2\eta t} \quad (\text{A24})$$

The total current operator can be written as a summation of diagonal and off-diagonal terms, *i.e.*, $\mathbf{j} = \mathbf{j}^{\text{dia}} + \mathbf{j}^{\text{off}}$

where, \mathbf{j}^{dia} and \mathbf{j}^{off} are defined as

$$\mathbf{j}^{\text{dia}} = \frac{e}{V} \sum_{n, \mathbf{k}} \mathbf{v}_{nn}(\mathbf{k}) \rho_{nn}^{(2)}(\mathbf{k}, t) \quad (\text{A25})$$

$$\mathbf{j}^{\text{off}} = \frac{e}{V} \sum_{n, m, n \neq m, \mathbf{k}} \mathbf{v}_{mn}(\mathbf{k}) \rho_{nm}^{(2)}(\mathbf{k}, t) \quad (\text{A26})$$

To calculate the diagonal contribution to the current operator, we replace the term $\lim_{\eta \rightarrow 0} \frac{-1}{2i\hbar\eta} \frac{1}{E_n(\mathbf{k}) - E_m(\mathbf{k}) + \hbar\omega - i\hbar\eta}$ by

$$\lim_{\eta \rightarrow 0} -\frac{\pi}{2\hbar\eta} \delta(E_n(\mathbf{k}) - E_m(\mathbf{k}) + \hbar\omega) - \frac{1}{2i\hbar\eta} \mathcal{P} \frac{1}{E_n(\mathbf{k}) - E_m(\mathbf{k}) + \hbar\omega} - \frac{1}{2} \mathcal{P} \frac{1}{(E_n(\mathbf{k}) - E_m(\mathbf{k}) + \hbar\omega)^2} \quad (\text{A27})$$

$$\begin{aligned} \mathbf{j}^{\text{dia1}} &= -\frac{e^3\pi}{2V\hbar\eta} \sum_{n,m,i,j,\omega,\mathbf{k}} (f_n^T(\mathbf{k}, \mu) - f_m^T(\mathbf{k}, \mu)) \mathbf{v}_{nn}(\mathbf{k}) (\mathbf{v} \cdot \mathbf{A})_{nl} (\mathbf{v} \cdot \mathbf{A})_{lm} \delta(E_n(\mathbf{k}) - E_m(\mathbf{k}) + \hbar\omega) \\ \mathbf{j}^{\text{dia2}} &= -\frac{e^3}{V2i\hbar\eta} \sum_{n,m,\mathbf{k}} (f_n^T(\mathbf{k}, \mu) - f_m^T(\mathbf{k}, \mu)) (\mathbf{v}_{nn}(\mathbf{k}) - \mathbf{v}_{mm}(\mathbf{k})) (\mathbf{v} \cdot \mathbf{A})_{nl} (\mathbf{v} \cdot \mathbf{A})_{lm} \frac{1}{E_n(\mathbf{k}) - E_m(\mathbf{k}) + \hbar\omega} \\ \mathbf{j}^{\text{dia3}} &= \frac{e^3}{V} \sum_{n,m,i,j,\omega,\mathbf{k}} (f_n^T(\mathbf{k}, \mu) - f_m^T(\mathbf{k}, \mu)) \times \mathcal{P} \frac{\mathbf{v}_{nn}(\mathbf{k}) - \mathbf{v}_{mm}(\mathbf{k})}{2(E_n(\mathbf{k}) - E_m(\mathbf{k}) + \hbar\omega)^2} (\mathbf{v} \cdot \mathbf{A})_{nm} (\mathbf{v} \cdot \mathbf{A})_{mn} \end{aligned}$$

For \mathbf{j}^{dia3} , the principal part in the above expression can

Using the above expression j^{dia} can be broken into three parts *i.e.*, $\mathbf{j}^{\text{dia}} = \mathbf{j}^{\text{dia1}} + \mathbf{j}^{\text{dia2}} + \mathbf{j}^{\text{dia3}}$. By using the above identity we obtain the three diagonal terms as

be replaced by $-\nabla_{\mathbf{k}} \mathcal{P} \frac{1}{2\hbar} \frac{1}{(E_n(\mathbf{k}) - E_m(\mathbf{k}) + \hbar\omega)}$ which reduces the term \mathbf{j}^{dia3} as

$$\mathbf{j}^{\text{dia3}} = \frac{e^3}{V2\hbar} \sum_{n,m,i,j,\omega,\mathbf{k}} (f_n^T(\mathbf{k}, \mu) - f_m^T(\mathbf{k}, \mu)) \times \nabla_{\mathbf{k}} \frac{1}{E_n(\mathbf{k}) - E_m(\mathbf{k}) + \hbar\omega} (\mathbf{v} \cdot \mathbf{A})_{nm} (\mathbf{v} \cdot \mathbf{A})_{mn} \quad (\text{A28})$$

The off-diagonal contribution to the current is given as

$$\begin{aligned} \mathbf{j}^{\text{off}} &= \frac{e}{V} \sum_{n,m,n \neq m} \mathbf{v}_{mn}(\mathbf{k}) \rho_{nm}^{(2)}(\mathbf{k}, \omega) \\ &= \frac{e^3 i}{V\hbar} \sum_{i,j,m,n,\mathbf{k},\omega} \frac{(f_m^T(\mathbf{k}, \mu) - f_l^T(\mathbf{k}, \mu)) (\mathbf{v} \cdot \mathbf{A})_{nl} (\mathbf{v} \cdot \mathbf{A})_{lm}}{(E_m(\mathbf{k}) - E_l(\mathbf{k}) + \hbar\omega_1 - i\hbar\eta)} \mathbf{r}_{mn}(\mathbf{k}) + \frac{(f_n^T(\mathbf{k}, \mu) - f_l^T(\mathbf{k}, \mu)) v_{nl}^j(\mathbf{k}) (\mathbf{v} \cdot \mathbf{A})_{nm} (\mathbf{v} \cdot \mathbf{A})_{mn}}{(E_n(\mathbf{k}) - E_l(\mathbf{k}) + \hbar\omega_1 - i\hbar\eta)} \mathbf{r}_{mn}(\mathbf{k}) \\ &+ \frac{e^3 i}{V\hbar} \sum_{i,j,m,n,\mathbf{k}} \frac{(f_m^T(\mathbf{k}, \mu) - f_l^T(\mathbf{k}, \mu)) v_{lm}^i(\mathbf{k})}{(E_m(\mathbf{k}) - E_l(\mathbf{k}) + \hbar\omega_1 - i\hbar\eta)} A_i(\omega) A_j(\omega) \int d\mathbf{k}' v_{nl}^{\mathbf{k}'\mathbf{k}} \mathbf{r}_{mn}^{\mathbf{k}\mathbf{k}'} + \frac{(f_n^T(\mathbf{k}, \mu) - f_l^T(\mathbf{k}, \mu)) v_{nl}^i(\mathbf{k})}{(E_m(\mathbf{k}) - E_l(\mathbf{k}) + \hbar\omega_1 - i\hbar\eta)} \int d\mathbf{k}' v_{lm}^{\mathbf{k}'\mathbf{k}} \mathbf{r}_{mn}^{\mathbf{k}\mathbf{k}'} \end{aligned} \quad (\text{A29})$$

where in the above expression the integration limits are from $\mathbf{k} - \epsilon$ to $\mathbf{k} + \epsilon$ and $\epsilon \rightarrow 0$. In the first line of Eq. A30, if we rotate the indices $l \rightarrow n$, $m \rightarrow l$ and $n \rightarrow m$, we get the term $[v_{mn}^j \mathbf{r}_{lm}, v_{lm}^j \mathbf{r}_{mn}]$ which turns out to be equal to 0 due to the commutation between \mathbf{r} and \mathbf{p} as $[r^i, v^j] = i\hbar\delta_{ij}$. In Eq. A30 we have written the velocity \mathbf{v} operator in terms of the position operator \mathbf{r} . To do this we use the definition of velocity operator to calculate its

matrix elements as [133]

$$\begin{aligned} v_{nm}(\mathbf{k}) &= \frac{i}{\hbar} \langle n | [H, \mathbf{r}] | m \rangle = \frac{i}{\hbar} [\langle n | H \mathbf{r} | \chi_m(\mathbf{k}) \rangle - \langle m | \mathbf{r} H | m \rangle] \\ &= \frac{i}{\hbar} (E_n(\mathbf{k}) - E_m(\mathbf{k})) \mathbf{r}_{nm}(\mathbf{k}) \end{aligned}$$

where $\mathbf{r}_{nm}(\mathbf{k})$ is defined as $r_{nm}^{\mathbf{k}\mathbf{k}'} = \langle n\mathbf{k} | \mathbf{r} | m\mathbf{k}' \rangle$. These

matrix elements are computed as

$$\begin{aligned} \mathbf{r}_{nm}(\mathbf{k}, \mathbf{k}') &= \langle n\mathbf{k} | \mathbf{r} | m\mathbf{k}' \rangle = \int d^d \mathbf{r} \langle n\mathbf{k} | \mathbf{r} \rangle \langle \mathbf{r} | m\mathbf{k}' \rangle \\ &= \int d^d \mathbf{r} u_{n\mathbf{k}}^*(\mathbf{r}) e^{-i\mathbf{k}\cdot\mathbf{r}} \mathbf{r} u_{m\mathbf{k}'}(\mathbf{r}) e^{i\mathbf{k}'\cdot\mathbf{r}} \\ &= \int d^d \mathbf{r} u_{n\mathbf{k}}^*(\mathbf{r}) e^{-i\mathbf{k}\cdot\mathbf{r}} u_{m\mathbf{k}'}(\mathbf{r}) (-i\nabla_{\mathbf{k}'} e^{i\mathbf{k}'\cdot\mathbf{r}}) \end{aligned}$$

Using simply the product rule of the gradient operator, it can further be rewritten as

$$\begin{aligned} \mathbf{r}_{nm}(\mathbf{k}, \mathbf{k}') &= \int d^d \mathbf{r} u_{n\mathbf{k}}^*(\mathbf{r}) e^{-i\mathbf{k}\cdot\mathbf{r}} \left\{ (-i\nabla_{\mathbf{k}'}) \left(u_{m\mathbf{k}'}(\mathbf{r}) e^{i\mathbf{k}'\cdot\mathbf{r}} \right) \right\} + \int d^d \mathbf{r} u_{n\mathbf{k}}^*(\mathbf{r}) e^{-i\mathbf{k}\cdot\mathbf{r}} \left\{ i e^{i\mathbf{k}'\cdot\mathbf{r}} \nabla_{\mathbf{k}'} u_{m\mathbf{k}'}(\mathbf{r}) \right\} \quad (\text{A30}) \\ &= (-i\nabla_{\mathbf{k}'}) \delta_{nm} (2\pi)^d \delta(\mathbf{k}' - \mathbf{k}) + \int d^d \mathbf{r} i e^{i(\mathbf{k}' - \mathbf{k})\cdot\mathbf{r}} u_{n\mathbf{k}}^*(\mathbf{r}) \nabla_{\mathbf{k}'} u_{m\mathbf{k}'}(\mathbf{r}) \\ &= (-i\nabla_{\mathbf{k}'}) \delta_{nm} (2\pi)^d \delta(\mathbf{k}' - \mathbf{k}) + (2\pi)^d \delta(\mathbf{k}' - \mathbf{k}) \mathbf{r}_{nm}(\mathbf{k}) \end{aligned}$$

From the above expression we see that, the first term vanishes if the band indices $n \neq m$. For identical band

indices, *i.e.*, for $n = m$, we integrate the above expression for $\mathbf{k} = \mathbf{k}'$

$$\int_{\mathbf{k}-\epsilon}^{\mathbf{k}+\epsilon} d^3 \mathbf{k}' g(\mathbf{k}') \mathbf{r}_{nn}^{\mathbf{k}, \mathbf{k}'} = i \nabla_{\mathbf{k}} g(\mathbf{k}) + g(\mathbf{k}) \mathbf{R}_{nn}(\mathbf{k}) \quad \text{and} \quad \int_{\mathbf{k}-\epsilon}^{\mathbf{k}+\epsilon} d^3 \mathbf{k}' g(\mathbf{k}') \mathbf{r}_{nn}^{\mathbf{k}', \mathbf{k}} = -i \nabla_{\mathbf{k}} g(\mathbf{k}) + g(\mathbf{k}) \mathbf{R}_{nn}(\mathbf{k}) \quad (\text{A31})$$

where \mathbf{r} has been replaced by \mathbf{R} . Using Eq. A31 in A30,

we obtain the expression for the off-diagonal contribution to the total current operator as

$$\mathbf{j}^{\text{off}} = \frac{e^3}{2V\hbar} \sum_{n,m,i,j,\mathbf{k}} \frac{f_m^T(\mathbf{k}, \mu) - f_n^T(\mathbf{k}, \mu)}{E_n(\mathbf{k}) - E_m(\mathbf{k}) + \hbar\omega} A_i(\omega) A_j(\omega) \left(v_{nm}^i(\mathbf{k}) \nabla_{\mathbf{k}} v_{mn}^j(\mathbf{k}) + (\mathbf{R}_{mm}(\mathbf{k}) - \mathbf{R}_{nn}(\mathbf{k})) v_{nm}^i(\mathbf{k}) v_{mn}^j(\mathbf{k}) \right) \quad (\text{A32})$$

Here i, j are the Cartesian coordinates and v_{mn}^i is the

i^{th} component of the velocity operator. By using the following identity

$$\lim_{\eta \rightarrow 0} \frac{1}{2i\hbar\eta} \frac{1}{E_n(\mathbf{k}) - E_m(\mathbf{k}) + \hbar\omega - i\hbar\eta} = \lim_{\eta \rightarrow 0} \frac{\pi}{2\hbar\eta} \delta(E_n(\mathbf{k}) - E_m(\mathbf{k}) + \hbar\omega) + \mathcal{P} \frac{1}{E_n(\mathbf{k}) - E_m(\mathbf{k}) + \hbar\omega} \quad (\text{A33})$$

We separate out the resonant (\mathbf{j}^{off1}) and non-resonant

contribution (\mathbf{j}^{off2}) to Eq. A28. Using the first term on the RHS of Eq. A33 in Eq. A32 gives the resonant contribution as

$$\mathbf{j}^{\text{off1}} = \frac{e^3 \pi}{V \hbar} \sum_{n,m,i,j,\mathbf{k}} (f_m^T(\mathbf{k}, \mu) - f_n^T(\mathbf{k}, \mu)) A_i(\omega) A_j(\omega) (v_{nm}^i(\mathbf{k}) \nabla_{\mathbf{k}} v_{mn}^j(\mathbf{k}) + (\mathbf{R}_{mm}(\mathbf{k}) - \mathbf{R}_{nn}(\mathbf{k})) v_{nm}^i v_{mn}^j) \delta(E_n(\mathbf{k}) - E_m(\mathbf{k}) + \hbar\omega) \quad (\text{A34})$$

The remaining non-resonant contribution related with principal part is given as

$$\mathbf{j}^{\text{off2}} = \frac{e^3 \pi}{V \hbar} \sum_{n,m,i,j,\mathbf{k}} (f_m^T(\mathbf{k}, \mu) - f_n^T(\mathbf{k}, \mu)) A_i(\omega) A_j(\omega) (v_{nm}^i(\mathbf{k}) \nabla_{\mathbf{k}} v_{mn}^j(\mathbf{k}) + (\mathbf{R}_{mm}(\mathbf{k}) - \mathbf{R}_{nn}(\mathbf{k})) v_{nm}^i v_{mn}^j) \mathcal{P} \frac{1}{E_n(\mathbf{k}) - E_m(\mathbf{k}) + \hbar\omega} \quad (\text{A35})$$

On adding the non-resonant contribution to the off-diagonal current and the diagonal term of $\mathbf{j}(t)$ given in Eq. A28 and the non resonant part of the off-diagonal term given in the above expression in which $(\mathbf{R}_{mm}(\mathbf{k}) - \mathbf{R}_{nn}(\mathbf{k})) v_{nm}^i v_{mn}^j$ vanishes, we obtain the contribution of the Fermi surface

$$\mathbf{j}^{\text{Fermi}} = \frac{e^3}{V \hbar} \sum_{n,m,\mathbf{k}} \nabla_{\mathbf{k}} [f_n^T(\mathbf{k}, \mu) - f_m^T(\mathbf{k}, \mu)] \quad (\text{A36})$$

$$\times \frac{(\mathbf{v} \cdot \mathbf{A})_{nm} (\mathbf{v} \cdot \mathbf{A})_{mn}}{E_n(\mathbf{k}) - E_m(\mathbf{k}) + \hbar\omega}$$

To evaluate $\mathbf{j}^{\text{Fermi}}$ in TBLG, we need to evaluate the expression given in Eq. A37 for all the pair of bands. The summation over \mathbf{k} includes all the \mathbf{k} -points in the MBZ. Below, we provide a brief explanation to demonstrate the behavior of $\nabla_{\mathbf{k}} [f_n^T(\mathbf{k}, \mu) - f_m^T(\mathbf{k}, \mu)]$. For our purpose, we rename the indices $n(m)$ by $c(v)$, where c stands for conduction and v stands for valence band index and write the term $\nabla_{\mathbf{k}} [f_c^T(\mathbf{k}, \mu) - f_v^T(\mathbf{k}, \mu)]$ as

$$\nabla_{\mathbf{k}}(F) = \nabla_{\mathbf{k}} \left(\frac{1}{e^{\beta(E_c(\mathbf{k})-\mu)} + 1} - \frac{1}{e^{\beta(E_v(\mathbf{k})-\mu)} + 1} \right)$$

$$= \frac{\partial}{\partial k_x} \left(\frac{1}{e^{\beta(E_c(\mathbf{k})-\mu)} + 1} - \frac{1}{e^{\beta(E_v(\mathbf{k})-\mu)} + 1} \right)$$

$$+ \frac{\partial}{\partial k_y} \left(\frac{1}{e^{\beta(E_c(\mathbf{k})-\mu)} + 1} - \frac{1}{e^{\beta(E_v(\mathbf{k})-\mu)} + 1} \right)$$

where, $\beta = 1/k_B T$, with k_B being the Boltzmann constant, T being the temperature and μ being the chemical potential. Depending on the position of μ , we demonstrate the behavior of the quantities appearing in the above expression at a single $\mathbf{k} = (k_x, k_y)$ point.

- If for a given \mathbf{k} , $E_c(\mathbf{k}) > \mu$, i.e $E_c(\mathbf{k}) - \mu = x$

$$\lim_{\beta \rightarrow \infty} \frac{\partial}{\partial k_x} \frac{1}{e^{\beta x} + 1} = \lim_{\beta \rightarrow \infty} \frac{-\beta e^{\beta x}}{(e^{\beta x} + 1)^2} \frac{\partial}{\partial k_x} E_c(\mathbf{k})$$

$$= \lim_{\beta \rightarrow \infty} \frac{x}{2x^2 e^{\beta x}}$$

$$= 0$$

Similarly, we can write

$$\frac{\partial}{\partial k_x} \left(\frac{1}{e^{\beta(E_c(\mathbf{k})-\mu)} + 1} - \frac{1}{e^{\beta(E_v(\mathbf{k})-\mu)} + 1} \right) - \quad (\text{A37})$$

$$\lim_{\beta \rightarrow \infty} \frac{\partial}{\partial k_x} \frac{1}{e^{\beta(E_v(\mathbf{k})-\mu)} + 1} = 0 \text{ for } E_v(\mathbf{k}) > \mu$$

- If for a given \mathbf{k} , $E_c(\mathbf{k}) < \mu$ i.e $E_c(\mathbf{k}) - \mu = -x$

$$\lim_{\beta \rightarrow \infty} \frac{\partial}{\partial k_x} \frac{1}{e^{-\beta x} + 1} = \lim_{\beta \rightarrow \infty} \frac{\beta e^{-\beta x}}{(e^{-\beta x} + 1)^2} \frac{\partial}{\partial k_x} E_c(\mathbf{k})$$

$$= 0$$

Similarly, we can show that $\lim_{\beta \rightarrow \infty} \frac{\partial}{\partial k_x} \frac{1}{e^{\beta(E_v(\mathbf{k})-\mu)} + 1} = 0$ for $E_v(\mathbf{k}) < \mu$

- If for a given \mathbf{k} , $E_c(\mathbf{k}) = \mu$ i.e $E_c(\mathbf{k}) - \mu = 0$

$$\lim_{\beta \rightarrow \infty} \frac{\partial}{\partial k_x} \frac{1}{e^{\beta(E_c(\mathbf{k})-\mu)} + 1} = \frac{\partial}{\partial k_x} E_c(\mathbf{k}) \lim_{\beta \rightarrow \infty} \frac{-\beta}{4}$$

$$= \frac{\partial}{\partial k_x} E_c(\mathbf{k}) \delta(E_c(\mathbf{k}) - \mu)$$

Similarly, we have $\lim_{\beta \rightarrow \infty} \frac{\partial}{\partial k_x} \frac{1}{e^{\beta(E_c(\mathbf{k})-\mu)} + 1} = \frac{\partial}{\partial k_x} E_v(\mathbf{k}) \delta(E_v(\mathbf{k}) - \mu)$

Based on this we conclude that the term $\nabla_{\mathbf{k}}(f_n^T(\mathbf{k}, \mu) - f_m^T(\mathbf{k}, \mu))$ appearing in Eq. A37 has a contribution from only those \mathbf{k} points at which either $E_c(\mathbf{k}) = \mu$ or $E_v(\mathbf{k}) = \mu$. Therefore the contribution appearing in the gradient term $\nabla_{\mathbf{k}} \left(\frac{1}{e^{\beta(E_c(\mathbf{k})-\mu)} + 1} - \frac{1}{e^{\beta(E_v(\mathbf{k})-\mu)} + 1} \right)$ can be replaced by

$$\nabla_{\mathbf{k}} E_c(\mathbf{k}) \delta(E_c(\mathbf{k}) - \mu) - \nabla_{\mathbf{k}} E_v(\mathbf{k}) \delta(E_v(\mathbf{k}) - \mu) \quad (\text{A38})$$

The variation of j^{Fermi} as function of $\hbar\omega$ is shown in Fig. 14. We see that as $\omega \rightarrow 0$, $j^{\text{Fermi}} \rightarrow \infty$.

Appendix B: The effect of corrugation, doping-dependent Hartree interactions and ph-asymmetry on the one-photon absorption coefficient

Bistrizter and MacDonald [27] evaluated the band structure of pristine TBLG by setting $w_0 = w_1$. This model was later modified to include the effects of corrugation [67], doping-dependent Hartree interactions [105–109] and particle-hole asymmetry [104, 106]. In FIG. 15 (a), we show how the bands alter by including these modifications. The behavior of α_1 for these four models is shown in FIG. 15 (b). We infer that the resonant features of α_1 (marked by the black arrows in

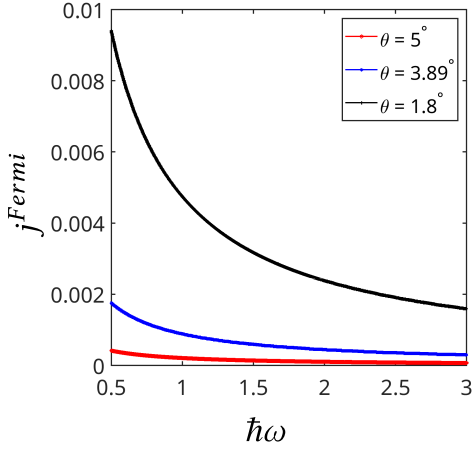


FIG. 14. j^{Fermi} as a function of $\hbar\omega$ for different twist angles

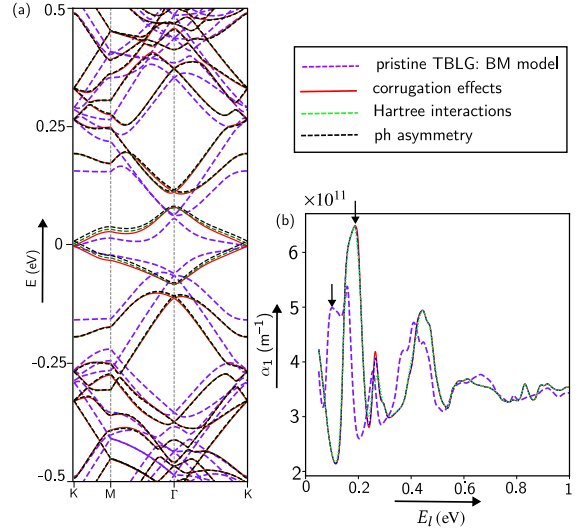


FIG. 15. The (a) band structure and (b) behavior of the one-photon absorption coefficient α_1 as a function of E_l for $\theta = 1.54^\circ$. The different colors indicate the step-wise modification added to the model as mentioned in the legend.

FIG. 15 (b) are strongly altered on including the corrugation effects in pristine TBLG. As a result, the peak energy increases from ~ 0.1 eV to ~ 0.185 eV. Any other modification in the system does not appreciably change the behavior of the α_1 as a function of E_l .

- [1] C. Berger, Z. Song, X. Li, X. Wu, N. Brown, C. Naud, D. Mayou, T. Li, J. Hass, A. N. Marchenkov, E. H. Conrad, P. N. First, and W. A. de Heer, Electronic confinement and coherence in patterned epitaxial graphene, *Science* **312**, 1191 (2006).
- [2] J. Hass, R. Feng, J. E. Millán-Otoya, X. Li, M. Sprinkle, P. N. First, W. A. de Heer, E. H. Conrad, and C. Berger, Structural properties of the multilayer graphene/ $4h$ -SiC(000 $\bar{1}$) system as determined by surface x-ray diffraction, *Phys. Rev. B* **75**, 214109 (2007).
- [3] R. Zhao, Y. Zhang, T. Gao, Y. Gao, N. Liu, L. Fu, and Z. Liu, Scanning tunneling microscope observations of non-ab stacking of graphene on ni films, *Nano Research* **4**, 712 (2011).
- [4] L. Xie, H. Wang, C. Jin, X. Wang, L. Jiao, K. Suenaga, and H. Dai, Graphene nanoribbons from unzipped carbon nanotubes: Atomic structures, raman spectroscopy, and electrical properties, *Journal of the American Chemical Society* **133**, 10394 (2011).
- [5] G. Li, A. Luican, J. M. B. Lopes dos Santos, A. H. Castro Neto, A. Reina, J. Kong, and E. Y. Andrei, Observation of van hove singularities in twisted graphene layers, *Nature Physics* **6**, 109 (2010).
- [6] D. L. Miller, K. D. Kubista, G. M. Rutter, M. Ruan, W. A. de Heer, P. N. First, and J. A. Stroscio, Structural analysis of multilayer graphene via atomic moiré interferometry, *Phys. Rev. B* **81**, 125427 (2010).
- [7] A. Luican, G. Li, A. Reina, J. Kong, R. R. Nair, K. S. Novoselov, A. K. Geim, and E. Y. Andrei, Single-layer behavior and its breakdown in twisted graphene layers, *Phys. Rev. Lett.* **106**, 126802 (2011).
- [8] I. Amidror, *The Theory of the Moiré Phenomenon*, edited by I. Amidror (Springer London, 2009).
- [9] L. Zou, H. C. Po, A. Vishwanath, and T. Senthil, Band structure of twisted bilayer graphene: Emergent symmetries, commensurate approximants, and wannier obstructions, *Phys. Rev. B* **98**, 085435 (2018).
- [10] M. Long, Z. Zhan, P. A. Pantaleón, J. A. Silva-Guillén, F. Guinea, and S. Yuan, Electronic properties of twisted bilayer graphene suspended and encapsulated with hexagonal boron nitride, *Phys. Rev. B* **107**, 115140 (2023).
- [11] Y. Wang, Z. Ni, L. Liu, Y. Liu, C. Cong, T. Yu, X. Wang, D. Shen, and Z. Shen, Stacking-dependent optical conductivity of bilayer graphene, *ACS Nano* **4**, 4074 (2010).
- [12] H. Patel, L. Huang, C.-J. Kim, J. Park, and M. W. Graham, Stacking angle-tunable photoluminescence from interlayer exciton states in twisted bilayer graphene, *Nature Communications* **10**, 1445 (2019).
- [13] T. V. Alencar, D. von Dreifus, M. G. C. Moreira, G. S. N. Eliel, C.-H. Yeh, P.-W. Chiu, M. A. Pimenta, L. M. Malard, and A. M. de Paula, Twisted bilayer graphene photoluminescence emission peaks at van hove singularities, *Journal of Physics: Condensed Matter* **30**,

- 175302 (2018).
- [14] X. Zou, J. Shang, J. Leaw, Z. Luo, L. Luo, C. La-o vorakiat, L. Cheng, S. A. Cheong, H. Su, J.-X. Zhu, Y. Liu, K. P. Loh, A. H. Castro Neto, T. Yu, and E. E. M. Chia, Terahertz conductivity of twisted bilayer graphene, *Phys. Rev. Lett.* **110**, 067401 (2013).
- [15] Z. H. Ni, T. Yu, Z. Q. Luo, Y. Y. Wang, L. Liu, C. P. Wong, J. Miao, W. Huang, and Z. X. Shen, Probing charged impurities in suspended graphene using raman spectroscopy, *ACS Nano* **3**, 569 (2009).
- [16] A. Righi, S. D. Costa, H. Chacham, C. Fantini, P. Venezuela, C. Magnuson, L. Colombo, W. S. Bacsa, R. S. Ruoff, and M. A. Pimenta, Graphene moiré patterns observed by umklapp double-resonance raman scattering, *Phys. Rev. B* **84**, 241409 (2011).
- [17] K. Sato, R. Saito, C. Cong, T. Yu, and M. S. Dresselhaus, Zone folding effect in raman g -band intensity of twisted bilayer graphene, *Phys. Rev. B* **86**, 125414 (2012).
- [18] J. T. Robinson, S. W. Schmucker, C. B. Diaconescu, J. P. Long, J. C. Culbertson, T. Ohta, A. L. Friedman, and T. E. Beechem, Electronic hybridization of large-area stacked graphene films, *ACS Nano* **7**, 637 (2013).
- [19] Y. Wang, Z. Su, W. Wu, S. Nie, N. Xie, H. Gong, Y. Guo, J. Hwan Lee, S. Xing, X. Lu, H. Wang, X. Lu, K. McCarty, S.-s. Pei, F. Robles-Hernandez, V. G. Hadjiev, and J. Bao, Resonance raman spectroscopy of g -line and folded phonons in twisted bilayer graphene with large rotation angles, *Applied Physics Letters* **103**, 123101 (2013).
- [20] E. Y. Andrei and A. H. MacDonald, Graphene bilayers with a twist, *Nat Mater* **19**, 1265 (2020).
- [21] D. Aggarwal, R. Narula, and S. Ghosh, A primer on twistrionics: a massless dirac fermion's journey to moiré patterns and flat bands in twisted bilayer graphene, *Journal of Physics: Condensed Matter* **35**, 143001 (2023).
- [22] Z. Ni, Y. Wang, T. Yu, Y. You, and Z. Shen, Reduction of fermi velocity in folded graphene observed by resonance raman spectroscopy, *Phys. Rev. B* **77**, 235403 (2008).
- [23] J. M. B. Lopes dos Santos, N. M. R. Peres, and A. H. Castro Neto, Graphene bilayer with a twist: Electronic structure, *Phys. Rev. Lett.* **99**, 256802 (2007).
- [24] E. Suárez Morell, J. D. Correa, P. Vargas, M. Pacheco, and Z. Barticevic, Flat bands in slightly twisted bilayer graphene: Tight-binding calculations, *Phys. Rev. B* **82**, 121407 (2010).
- [25] S. Shallcross, S. Sharma, and O. A. Pankratov, Quantum interference at the twist boundary in graphene, *Phys. Rev. Lett.* **101**, 056803 (2008).
- [26] S. Shallcross, S. Sharma, E. Kandelaki, and O. A. Pankratov, Electronic structure of turbostratic graphene, *Phys. Rev. B* **81**, 165105 (2010).
- [27] R. Bistritzer and A. H. MacDonald, Moiré bands in twisted double-layer graphene, *Proceedings of the National Academy of Sciences* **108**, 12233 (2011).
- [28] J. M. B. Lopes dos Santos, N. M. R. Peres, and A. H. Castro Neto, Continuum model of the twisted graphene bilayer, *Phys. Rev. B* **86**, 155449 (2012).
- [29] G. Trambly de Laissardière, D. Mayou, and L. Magaud, Localization of dirac electrons in rotated graphene bilayers, *Nano Letters* **10**, 804 (2010).
- [30] D. V. Chichinadze, L. Classen, and A. V. Chubukov, Nematic superconductivity in twisted bilayer graphene, *Phys. Rev. B* **101**, 224513 (2020).
- [31] Y. Cao, V. Fatemi, S. Fang, K. Watanabe, T. Taniguchi, E. Kaxiras, and P. Jarillo-Herrero, Unconventional superconductivity in magic-angle graphene superlattices, *Nature* **556**, 43 (2018).
- [32] Y. Choi, J. Kemmer, Y. Peng, A. Thomson, H. Arora, R. Polski, Y. Zhang, H. Ren, J. Alicea, G. Refael, F. von Oppen, K. Watanabe, T. Taniguchi, and S. Nadj-Perge, Electronic correlations in twisted bilayer graphene near the magic angle, *Nature Physics* **15**, 1174 (2019).
- [33] Y. Cao, V. Fatemi, A. Demir, S. Fang, S. L. Tomarken, J. Y. Luo, J. D. Sanchez-Yamagishi, K. Watanabe, T. Taniguchi, E. Kaxiras, R. C. Ashoori, and P. Jarillo-Herrero, Correlated insulator behaviour at half-filling in magic-angle graphene superlattices, *Nature* **556**, 80 (2018).
- [34] Y.-Z. You and A. Vishwanath, Superconductivity from valley fluctuations and approximate $so(4)$ symmetry in a weak coupling theory of twisted bilayer graphene, *npj Quantum Materials* **4**, 16 (2019).
- [35] B. Roy and V. Juričić, Unconventional superconductivity in nearly flat bands in twisted bilayer graphene, *Phys. Rev. B* **99**, 121407 (2019).
- [36] H. C. Po, L. Zou, A. Vishwanath, and T. Senthil, Origin of mott insulating behavior and superconductivity in twisted bilayer graphene, *Phys. Rev. X* **8**, 031089 (2018).
- [37] C. Xu and L. Balents, Topological superconductivity in twisted multilayer graphene, *Phys. Rev. Lett.* **121**, 087001 (2018).
- [38] S. Fang and E. Kaxiras, Electronic structure theory of weakly interacting bilayers, *Phys. Rev. B* **93**, 235153 (2016).
- [39] G. Trambly de Laissardière, D. Mayou, and L. Magaud, Numerical studies of confined states in rotated bilayers of graphene, *Phys. Rev. B* **86**, 125413 (2012).
- [40] L. Krauss-Kodytek, W.-R. Hannes, T. Meier, C. Ruppert, and M. Betz, Nondegenerate two-photon absorption in znse: Experiment and theory, *Phys. Rev. B* **104**, 085201 (2021).
- [41] V. Nathan, A. H. Guenther, and S. S. Mitra, Review of multiphoton absorption in crystalline solids, *J. Opt. Soc. Am. B* **2**, 294 (1985).
- [42] J. H. Yee, Four-photon transition in semiconductors, *Phys. Rev. B* **3**, 355 (1971).
- [43] A. F. Gibson, C. B. Hatch, P. N. D. Maggs, D. R. Tilley, and A. C. Walker, Two-photon absorption in indium antimonide and germanium, *Journal of Physics C: Solid State Physics* **9**, 3259 (1976).
- [44] M. Bass, E. W. Van Stryland, and A. F. Stewart, Laser calorimetric measurement of two-photon absorption, *Applied Physics Letters* **34**, 142 (2008).
- [45] E. Girlanda, Two-photon absorption in semiconductors in a magnetic field, *Il Nuovo Cimento B (1971-1996)* **6**, 53 (1971).
- [46] R. R. Nair, P. Blake, A. N. Grigorenko, K. S. Novoselov, T. J. Booth, T. Stauber, N. M. R. Peres, and A. K. Geim, Fine structure constant defines visual transparency of graphene, *Science* **320**, 1308 (2008).
- [47] K. F. Mak, M. Y. Sfeir, Y. Wu, C. H. Lui, J. A. Misewich, and T. F. Heinz, Measurement of the optical conductivity of graphene, *Phys. Rev. Lett.* **101**, 196405

- (2008).
- [48] L. M. Zhang, Z. Q. Li, D. N. Basov, M. M. Fogler, Z. Hao, and M. C. Martin, Determination of the electronic structure of bilayer graphene from infrared spectroscopy, *Phys. Rev. B* **78**, 235408 (2008).
- [49] Z. Q. Li, E. A. Henriksen, Z. Jiang, Z. Hao, M. C. Martin, P. Kim, H. L. Stormer, and D. N. Basov, Band structure asymmetry of bilayer graphene revealed by infrared spectroscopy, *Phys. Rev. Lett.* **102**, 037403 (2009).
- [50] K. F. Mak, M. Y. Sfeir, J. A. Misewich, and T. F. Heinz, The evolution of electronic structure in few-layer graphene revealed by optical spectroscopy, *Proceedings of the National Academy of Sciences* **107**, 14999 (2010).
- [51] M. Orlita, C. Faugeras, J. M. Schneider, G. Martinez, D. K. Maude, and M. Potemski, Graphite from the viewpoint of Landau level spectroscopy: An effective graphene bilayer and monolayer, *Phys. Rev. Lett.* **102**, 166401 (2009).
- [52] M. Rumi and J. W. Perry, Two-photon absorption: an overview of measurements and principles, *Adv. Opt. Photon.* **2**, 451 (2010).
- [53] R. Braunstein and N. Ockman, Optical double-photon absorption in cds, *Phys. Rev.* **134**, A499 (1964).
- [54] U. M. Grassano, Two-photon spectroscopy in insulating crystals, in *Optical Properties of Excited States in Solids*, edited by B. Di Bartolo and C. Beckwith (Springer US, Boston, MA, 1992) pp. 643–659.
- [55] A. Saïssy, A. Azema, J. Botineau, and F. Gires, Absolute measurement of the 1.06 μm two-photon absorption coefficient in GaAs, *Applied physics* **15**, 99 (1978).
- [56] D. Sun, C. Divin, J. Rioux, J. E. Sipe, C. Berger, W. A. de Heer, P. N. First, and T. B. Norris, Coherent control of ballistic photocurrents in multilayer epitaxial graphene using quantum interference, *Nano Letters* **10**, 1293 (2010).
- [57] Q. Cui and H. Zhao, Coherent control of nanoscale ballistic currents in transition metal dichalcogenide res2, *ACS Nano* **9**, 3935 (2015).
- [58] I. Perez-Arjona, G. de Valcarcel, and E. Roldán, Two-photon absorption, *Revista Mexicana de Fisica* **49**, 92 (2003).
- [59] S. Maruo and S. Kawata, Two-photon-absorbed photopolymerization for three-dimensional microfabrication, in *Proceedings IEEE The Tenth Annual International Workshop on Micro Electro Mechanical Systems. An Investigation of Micro Structures, Sensors, Actuators, Machines and Robots* (1997) pp. 169–174.
- [60] C. Corredor, Z.-L. Huang, and K. Belfield, Two-photon 3d optical data storage via fluorescence modulation of an efficient fluorene dye by a photochromic diarylethene, *Advanced Materials* **18**, 2910 (2006).
- [61] D. A. Parthenopoulos and P. M. Rentzepis, Three-dimensional optical storage memory, *Science* **245**, 843 (1989).
- [62] M. Pawlicki, H. Collins, R. Denning, and H. Anderson, Two-photon absorption and the design of two-photon dyes, *Angewandte Chemie International Edition* **48**, 3244 (2009).
- [63] W. Denk, J. H. Strickler, and W. W. Webb, Two-photon laser scanning fluorescence microscopy, *Science* **248**, 73 (1990).
- [64] G. S. He, L.-S. Tan, Q. Zheng, and P. N. Prasad, Multiphoton absorbing materials: molecular designs, characterizations, and applications, *Chemical Reviews* **108**, 1245 (2008).
- [65] K. F. Lee, K. J. Kubarych, A. Bonvalet, and M. Joffe, Characterization of mid-infrared femtosecond pulses, *J. Opt. Soc. Am. B* **25**, A54 (2008).
- [66] M. Piccardo, N. A. Rubin, L. Meadowcroft, P. Chevalier, H. Yuan, J. Kimchi, and F. Capasso, Mid-infrared two-photon absorption in an extended-wavelength InGaAs photodetector, *Applied Physics Letters* **112**, 041106 (2018).
- [67] M. Koshino, N. F. Q. Yuan, T. Koretsune, M. Ochi, K. Kuroki, and L. Fu, Maximally localized Wannier orbitals and the extended Hubbard model for twisted bilayer graphene, *Phys. Rev. X* **8**, 031087 (2018).
- [68] R. W. Hellwarth, Theory of stimulated Raman scattering, *Phys. Rev.* **130**, 1850 (1963).
- [69] D. J. Gardiner, Introduction to Raman scattering, in *Practical Raman Spectroscopy*, edited by D. J. Gardiner and P. R. Graves (Springer Berlin Heidelberg, Berlin, Heidelberg, 1989) pp. 1–12.
- [70] A. V. Fedorov, A. V. Baranov, and K. Inoue, Two-photon transitions in systems with semiconductor quantum dots, *Phys. Rev. B* **54**, 8627 (1996).
- [71] L. El Chaar, L. Lamont, and N. El Zein, Review of photovoltaic technologies, *Renewable and Sustainable Energy Reviews* **15**, 2165 (2011).
- [72] A. Dutta and M. S. Islam, Novel broadband photodetector for optical communication, *Proceedings of SPIE - The International Society for Optical Engineering* **Phone**, 282 (2005).
- [73] M. Mahesh, The essential physics of medical imaging, third edition, *Med Phys* **40** (2013).
- [74] E. Malić, M. Hirtschulz, F. Milde, A. Knorr, and S. Reich, Analytical approach to optical absorption in carbon nanotubes, *Phys. Rev. B* **74**, 195431 (2006).
- [75] H. Haug and S. W. Koch, *Quantum Theory of the Optical and Electronic Properties of Semiconductors*, 5th ed. (WORLD SCIENTIFIC, 2009) <https://www.worldscientific.com/doi/pdf/10.1142/7184>.
- [76] Y. Wang, M. Tokman, and A. Belyanin, Second-order nonlinear optical response of graphene, *Phys. Rev. B* **94**, 195442 (2016).
- [77] L. Gao, Z. Addison, E. J. Mele, and A. M. Rappe, Intrinsic Fermi-surface contribution to the bulk photovoltaic effect, *Phys. Rev. Res.* **3**, L042032 (2021).
- [78] M. Göppert-Mayer, Elementary processes with two quantum transitions, *Annalen der Physik* **18**, 466 (2009).
- [79] C. Cohen-Tannoudji, G. Grynberg, and J. Dupont-Roc, *Atom-Photon Interactions: Basic Processes and Applications* (Wiley, New York, 1992).
- [80] X.-M. Qiu, N. Yang, W. Chu, and J.-Y. Yan, Detection of the chirality of twisted bilayer graphene by the optical absorption, *Phys. Rev. B* **109**, 125419 (2024).
- [81] M. K. Brinkley, D. S. L. Abergel, and B. D. Clader, Two-photon absorption in gapped bilayer graphene with a tunable chemical potential, *Journal of Physics: Condensed Matter* **28**, 365001 (2016).
- [82] K. Forbes, D. Bradshaw, and D. Andrews, Identifying diamagnetic interactions in scattering and nonlinear optics, *Physical Review A* **94** (2016).
- [83] C. R. Cosens, A balance-detector for alternating-current bridges, *Proceedings of the Physical Society* **46**, 818 (1934).

- [84] W. C. Michels, A Double Tube Vacuum Tube Voltmeter, *Review of Scientific Instruments* **9**, 10 (1938).
- [85] W. C. Michels and N. L. Curtis, A Pentode Lock-In Amplifier of High Frequency Selectivity, *Review of Scientific Instruments* **12**, 444 (1941).
- [86] R. Fitzpatrick, *Quantum Mechanics* (WORLD SCIENTIFIC, 2015).
- [87] J. M. Ralston and R. K. Chang, OPTICAL LIMITING IN SEMICONDUCTORS, *Applied Physics Letters* **15**, 164 (2003).
- [88] D. A. Kleinman, R. C. Miller, and W. A. Nordland, Two-photon absorption of Nd laser radiation in GaAs, *Applied Physics Letters* **23**, 243 (2003).
- [89] R. G. Wenzel, G. P. Arnold, and N. R. Greiner, Non-linear loss in ge in the 2.5–4- μ m range, *Appl. Opt.* **12**, 2245 (1973).
- [90] A. Penzkofer, W. Falkenstein, and W. Kaiser, Vibronic relaxation in the s1 state of rhodamine dye solutions, *Chemical Physics Letters* **44**, 82 (1976).
- [91] A. Penzkofer and W. Falkenstein, Three-photon absorption and subsequent excited-state absorption in cds, *Optics Communications* **16**, 247 (1976).
- [92] J. H. Bechtel and W. L. Smith, Two-photon absorption in semiconductors with picosecond laser pulses, *Phys. Rev. B* **13**, 3515 (1976).
- [93] I. M. Catalano, A. Cingolani, and A. Minafra, Transmittance, luminescence, and photocurrent in cds under two-photon excitation, *Phys. Rev. B* **9**, 707 (1974).
- [94] A. M. Johnston, C. R. Pidgeon, and J. Dempsey, Frequency dependence of two-photon absorption in insb and $\text{Hg}_{1-x}\text{Cd}_x\text{Te}$, *Phys. Rev. B* **22**, 825 (1980).
- [95] I. M. Catalano, A. Cingolani, and A. Minafra, Multiphoton transitions in ionic crystals, *Phys. Rev. B* **5**, 1629 (1972).
- [96] A. Miller, A. Johnston, J. Dempsey, J. Smith, C. R. Pidgeon, and G. D. Holah, Two-photon absorption in insb and $\text{Hg}_{1-x}\text{Cd}_x\text{Te}$, *Journal of Physics C: Solid State Physics* **12**, 4839 (1979).
- [97] M. Sheik-Bahae, A. Said, T.-H. Wei, D. Hagan, and E. Van Stryland, Sensitive measurement of optical nonlinearities using a single beam, *IEEE Journal of Quantum Electronics* **26**, 760 (1990).
- [98] B. Vest, E. Lucas, J. Jaek, R. Haidar, and E. Rosencher, Linear detection of sub-bandgap energy photons in silicon: A photo-assisted shockley-read mechanism (2013) pp. 1–1.
- [99] R. Bistritzer and A. H. MacDonald, Moiré butterflies in twisted bilayer graphene, *Phys. Rev. B* **84**, 035440 (2011).
- [100] Z. F. Wang, F. Liu, and M. Y. Chou, Fractal landau-level spectra in twisted bilayer graphene, *Nano Letters* **12**, 3833 (2012).
- [101] C. Zhou, X. Feng, and R. Gong, Angle-tunable two-photon absorption in twisted graphene systems, *Physica E: Low-dimensional Systems and Nanostructures* **140**, 115204 (2022).
- [102] G. Tarnopolsky, A. J. Kruchkov, and A. Vishwanath, Origin of magic angles in twisted bilayer graphene, *Phys. Rev. Lett.* **122**, 106405 (2019).
- [103] Z.-D. Song, B. Lian, N. Regnault, and B. A. Bernevig, Twisted bilayer graphene. ii. stable symmetry anomaly, *Phys. Rev. B* **103**, 205412 (2021).
- [104] J. Kang and O. Vafeek, Pseudomagnetic fields, particle-hole asymmetry, and microscopic effective continuum hamiltonians of twisted bilayer graphene, *Phys. Rev. B* **107**, 075408 (2023).
- [105] Z. A. H. Goodwin, V. Vitale, X. Liang, A. A. Mostofi, and J. Lischner, Hartree theory calculations of quasiparticle properties in twisted bilayer graphene, *Electronic Structure* **2**, 034001 (2020).
- [106] L. Rademaker, D. A. Abanin, and P. Mellado, Charge smoothening and band flattening due to hartree corrections in twisted bilayer graphene, *Phys. Rev. B* **100**, 205114 (2019).
- [107] T. Cea, N. R. Walet, and F. Guinea, Electronic band structure and pinning of fermi energy to van hove singularities in twisted bilayer graphene: A self-consistent approach, *Phys. Rev. B* **100**, 205113 (2019).
- [108] T. Cea, P. A. Pantaleón, N. R. Walet, and F. Guinea, Electrostatic interactions in twisted bilayer graphene, *Nano Materials Science* **4**, 27 (2022), special issue on Graphene and 2D Alternative Materials.
- [109] F. Guinea and N. R. Walet, Electrostatic effects, band distortions, and superconductivity in twisted graphene bilayers, *Proceedings of the National Academy of Sciences* **115**, 13174 (2018).
- [110] J. Jung and A. H. MacDonald, Accurate tight-binding models for the π bands of bilayer graphene, *Phys. Rev. B* **89**, 035405 (2014).
- [111] S. Carr, S. Fang, Z. Zhu, and E. Kaxiras, Exact continuum model for low-energy electronic states of twisted bilayer graphene, *Phys. Rev. Res.* **1**, 013001 (2019).
- [112] D. Arora, D. Aggarwal, S. Ghosh, and R. Narula, Interference effects in polarization-controlled rayleigh scattering in twisted bilayer graphene, *Phys. Rev. B* **107**, 205423 (2023).
- [113] H. Yang, X. Feng, Q. Wang, H. Huang, W. Chen, A. T. S. Wee, and W. Ji, Giant two-photon absorption in bilayer graphene, *Nano Letters* **11**, 2622 (2011).
- [114] R. Narula, N. Bonini, N. Marzari, and S. Reich, Dominant phonon wavevectors of the 2d raman mode of graphene, *physica status solidi (b)* **248**, 2635 (2011).
- [115] R. Narula, *Resonant Raman scattering in graphene*, Ph.D. thesis, Massachusetts Institute of Technology, Department of Materials Science and Engineering (2011).
- [116] X. Zheng, Y. Zhang, R. Chen, X. Cheng, Z. Xu, and T. Jiang, Z-scan measurement of the nonlinear refractive index of monolayer WS_2 , *Opt. Express* **23**, 15616 (2015).
- [117] Y. Li, N. Dong, S. Zhang, X. Zhang, Y. Feng, K. Wang, L. Zhang, and J. Wang, Giant two-photon absorption in monolayer MoS_2 , *Laser & Photonics Reviews* **9**, 427 (2015).
- [118] Y. Xie, S. Zhang, Y. Li, N. Dong, X. Zhang, L. Wang, W. Liu, I. M. Kislyakov, J.-M. Nunzi, H. Qi, L. Zhang, and J. Wang, Layer-modulated two-photon absorption in MoS_2 : probing the shift of the excitonic dark state and band-edge, *Photon. Res.* **7**, 762 (2019).
- [119] R. I. Woodward and E. J. R. Kelleher, 2d saturable absorbers for fibre lasers, *Applied Sciences* **5**, 1440 (2015).
- [120] W. Liu, M. Liu, Y. OuYang, H. Hou, G. Ma, M. Lei, and Z. Wei, Tungsten diselenide for mode-locked erbium-doped fiber lasers with short pulse duration, *Nanotechnology* **29**, 174002 (2018).
- [121] Zhou *et al.* [134] calculated the TPA coefficient by only considering the two-band projection limited to the vicinity of the Dirac point. Their results showed an absence of any resonant feature in α_2 .

- [122] J. Kang, H.-D. Yang, B. S. Joo, J.-S. Park, S. ee Lee, S. Jeong, J. Kyhm, M. Han, J. D. Song, and I. K. Han, Quantum cascade lasers with Y_2O_3 insulation layer operating at 8.1 μm , *Opt. Express* **25**, 19561 (2017).
- [123] P. Dean, A. Valavanis, J. Keeley, K. Bertling, Y. L. Lim, R. Alhathloul, A. D. Burnett, L. H. Li, S. P. Khanna, D. Indjin, T. Taimre, A. D. Rakić, E. H. Linfield, and A. G. Davies, Terahertz imaging using quantum cascade lasers—a review of systems and applications, *Journal of Physics D: Applied Physics* **47**, 374008 (2014).
- [124] Y.-P. Chang, A. J. Merer, H.-H. Chang, L.-J. Jhang, W. Chao, and J. J.-M. Lin, High resolution quantum cascade laser spectroscopy of the simplest criegee intermediate, ch_2oo , between 1273 cm^{-1} and 1290 cm^{-1} , *The Journal of Chemical Physics* **146**, 244302 (2017).
- [125] A. Deyasi, Electronic band structure of quantum cascade laser, in *Quantum Cascade Lasers*, edited by V. N. Stavrou (IntechOpen, Rijeka, 2017) Chap. 2.
- [126] J. C. Slater and G. F. Koster, Simplified lcao method for the periodic potential problem, *Phys. Rev.* **94**, 1498 (1954).
- [127] L. D. Landau and L. M. Lifshitz, *Quantum Mechanics Non-Relativistic Theory, Third Edition: Volume 3*, 3rd ed. (Butterworth-Heinemann, 1981).
- [128] J. E. Sipe and A. I. Shkrebtii, Second-order optical response in semiconductors, *Phys. Rev. B* **61**, 5337 (2000).
- [129] D. E. Parker, T. Morimoto, J. Orenstein, and J. E. Moore, Diagrammatic approach to nonlinear optical response with application to weyl semimetals, *Phys. Rev. B* **99**, 045121 (2019).
- [130] R. W. Boyd, Chapter 6 - nonlinear optics in the two-level approximation, in *Nonlinear Optics (Third Edition)*, edited by R. W. Boyd (Academic Press, Burlington, 2008) third edition ed., pp. 277–328.
- [131] C. Weber, *Optical Dynamics in Low-Dimensional Semiconductor Heterostructures. Quantum Dots and Quantum Cascade Lasers*, Ph.D. thesis (2008).
- [132] Absorption spectrum of graphene, in *Graphene and Carbon Nanotubes* (John Wiley and Sons, Ltd, 2013) Chap. 7, pp. 215–222.
- [133] F. de Juan, Y. Zhang, T. Morimoto, Y. Sun, J. E. Moore, and A. G. Grushin, Difference frequency generation in topological semimetals, *Phys. Rev. Res.* **2**, 012017 (2020).
- [134] C. Zhou, X. Feng, and R. Gong, Angle-tunable two-photon absorption in twisted graphene systems, *Physica E: Low-dimensional Systems and Nanostructures* **140**, 115204 (2022).